HHS Public Access

Author manuscript

Nat Immunol. Author manuscript; available in PMC 2024 March 01.

Published in final edited form as:

Nat Immunol. 2023 September ; 24(9): 1527–1539. doi:10.1038/s41590-023-01578-y.

Hallmarks of CD8 T cell dysfunction are established within hours of tumor antigen encounter prior to cell division

Michael W. Rudloff[1], **Paul Zumbo**[2,3], **Natalie R. Favret**[1], **Jessica J. Roetman**[1], **Carlos R. Detrés Román**[1], **Megan M. Erwin**[1], **Kristen A. Murray**[1], **Sriya T. Jonnakuti**[1], **Friederike Dündar**[2,3], **Doron Betel**[3,4,5], **Mary Philip**[1,6,7]

[1]Department of Medicine, Division of Hematology and Oncology, Department of Pathology, Microbiology, and Immunology, Vanderbilt School of Medicine, Nashville, TN, USA

[2]Department of Physiology and Biophysics, Weill Cornell Medicine, New York, NY, USA

[3]Applied Bioinformatics Core, Weill Cornell Medicine, New York, NY, USA

[4]Institute for Computational Biomedicine, Weill Cornell Medicine, New York, NY, USA

[5]Division of Hematology and Medical Oncology, Department of Medicine, Weill Cornell Medicine, New York, NY USA

[6]Vanderbilt Center for Immunobiology, Vanderbilt University Medical Center, Nashville, TN USA

[7]Vanderbilt-Ingram Cancer Center, Vanderbilt University Medical Center, Nashville, TN, USA

Abstract

Tumor-specific CD8 T cells (TST) in patients with cancer are dysfunctional and unable to halt cancer progression. TST dysfunction, also known as exhaustion, is thought to be driven by chronic antigen/T cell receptor (TCR) stimulation over days to weeks. However, we know little about the interplay between CD8 T cell function, cell division, and epigenetic remodeling within hours of activation. Here, we assessed early CD8 T cell differentiation, cell division, chromatin accessibility, and transcription in tumor-bearing mice and acutely-infected mice. Surprisingly, despite robust activation and proliferation, TST had near complete effector function impairment even prior to undergoing cell division, and had acquired hallmark chromatin accessibility features previously associated with later dysfunction/exhaustion. Moreover, continued tumor/antigen exposure drove progressive epigenetic remodeling, “imprinting” the dysfunctional state. Our study reveals the rapid divergence of T cell fate choice prior to cell division in the context of tumors versus infection.

CORRESPONDENCE: mary.philip@vumc.org.

AUTHOR CONTRIBUTIONS STATEMENT

M.W.R and M.P. conceived and designed the study and analyzed and interpreted data. M.W.R. carried out experiments, assisted by N.R.F., J.J.R., C.R.D.R, M.M.E, K.A.M, and S.T.J. P.Z., F.D., and D.B. designed and performed computational analyses of RNA-SEQ and ATAC-SEQ data. M.W.R. and M.P. wrote the manuscript, with all authors contributing to the writing and providing feedback.

CODE AVAILABILITY

Code has been deposited in GitHub: https://github.com/abcwcm/Rudloff2022.

COMPETING INTERESTS STATEMENT

The authors declare no competing interests.

CD8 T cell differentiation during acute infection has been well characterized: naive CD8 T cells encountering cognate antigen are activated, proliferate and undergo clonal expansion, and acquire the ability to produce effector cytokines (IFNγ, TNF) and cytolytic molecules (granzyme B; GZMB, perforin; PRF1)[1]. During chronic infection, CD8 T cells similarly undergo clonal expansion and initially acquire effector function, but with persistent antigen stimulation, undergo hierarchical loss of effector function and proliferative capacity, upregulate inhibitory receptors (e.g. PD1 and LAG3), and become exhausted[2]. Tumor-specific CD8 T cells (TST) found in progressing tumors also lack effector function and express inhibitory receptors; this dysfunction/exhaustion was attributed to persistent exposure to tumor antigen and the immunosuppressive tumor microenvironment over days to weeks. We and others have since demonstrated that T cell dysfunction can be observed within a few days of tumor antigen encounter[3, 4, 5]. However, the precise kinetics of how TST are activated, lose effector function, and first acquire epigenetic features of dysfunction/exhaustion is not known and has not been assessed *in vivo*.

In metazoans, proliferation and differentiation must be carefully regulated during embryogenesis and throughout life in order to ensure adequate cell numbers and organ function[6]. In immune cells such as developing thymocytes[7], helper T cells[8], and B cells[9, 10], proliferation has been shown to be required for differentiation to proceed. During acute infection, 24 hours of antigen stimulation is sufficient to set CD8 T cells on an antigen-independent proliferation and differentiation path to functional effector and memory states[11, 12, 13]. This “autopilot” differentiation[14] suggests that the initial 24 hours after activation is a critical window in which CD8 T cell fate is determined. However, it is unknown whether a similar autopilot differentiation occurs in tumors, driving T cells into a dysfunctional state.

To address this question, we utilized our established autochthonous model of liver carcinogenesis, in which TST can be tracked longitudinally over hours, days, and weeks during tumor development[15]. We previously identified critical features of tumor-induced CD8 T cell dysfunction/exhaustion (reviewed in [16]) in this model, including transcription factor (TF) expression changes such as TCF1 downregulation and TOX upregulation, inhibitory receptor expression (PD1, LAG3, CD39), and dysfunction/exhaustion-associated epigenetic and transcriptional hallmarks[5, 17]. Therefore, we leveraged our ability to track TST cell division and differentiation with temporal precision in tumor-bearing hosts. We found that CD8 T cells activated in mice with established liver tumors underwent similar rapid activation and proliferation as T cells during acute infection. However, CD8 T cells activated in tumor-bearing hosts were severely functionally impaired within 24 hours of activation, challenging the paradigm that chronic stimulation over days drives TST dysfunction. In contrast, CD8 T cells activated in infected mice could make effector cytokines and cytolytic molecules even prior to cell division. Furthermore, even fully functional committed effector CD8 T cells rapidly lost cytokine and cytotoxic function upon transfer into mice with liver tumors, demonstrating that negative regulatory signals in tumor-bearing hosts can override functional programming. We made similar findings in a pulmonary metastatic melanoma model with CD8 T cells of different antigen specificity, demonstrating that the impact of the late-stage tumors is not dependent on the tumor origin, tissue, or antigen specificity.

We profiled transcriptional and chromatin accessibility changes in CD8 T cells activated in infected mice or tumor-bearing mice at early pre-division time points. Congruous with our functional and immunophenotypic assessment, within 24 hours of activation in tumors, TST had acquired epigenetic hallmarks previously associated with later-stage dysfunction/exhaustion. We removed TST from tumors after increasing intervals of initial tumor exposure and assessed function and chromatin accessibility after parking in tumor/antigen-free hosts. With increasing initial tumor exposure time, TST had greater retention of tumor/dysfunction-associated chromatin accessibility features. Our studies demonstrate that TST acquire dysfunctional hallmarks, including chromatin accessibility changes, within hours of activation in late-stage tumor-bearing hosts, even prior to undergoing cell division, with dysfunction hallmarks and epigenetic programs stabilized/imprinted with continued tumor/antigen exposure.

RESULTS

TST robustly activate/proliferate but lack effector function

To determine the relationship between proliferation and differentiation to the functional or dysfunctional state, we labeled naive SV40 large T antigen (TAG)-specific CD8 T cells (TCR_{TAG}) with carboxyfluorescein succinimidyl ester (CFSE), allowing cell division tracking, and transferred them into mice with TAG-driven liver tumors (ASTxAlb-Cre), or into TAG epitope-expressing *L. monocytogenes* (LM_{TAG})-infected C57BL/6 mice (B6) (Fig. 1a). We analyzed TCR_{TAG} 12, 36, 48, and 60 hours (h) after transfer to capture T cells at all stages of division (Fig. 1b). T cells in both tumor-bearing (T) and infected hosts (E) underwent remarkably robust cell division (6+ divisions within 60h) (Fig. 1b, c), expanded (Extended Data Fig. 1b), and upregulated activation markers CD69 and CD44 (Extended Data Fig. 1a and Fig. 1b). Both E-TCR_{TAG} and T-TCR_{TAG} upregulated LAG3 and PD1, reflecting active TCR signaling[18, 19] (Fig. 1b and Extended Data Fig. 1a). T-TCR_{TAG} in tumors, tumor draining lymph nodes (tdLN), and spleens of ASTxAlb-Cre hosts showed similar proliferation and immunophenotypic changes (Extended Data Fig. 1a). Surprisingly, despite robust activation and proliferation, T-TCR_{TAG} completely failed to produce IFNγ and TNF in response to TAG peptide restimulation *ex vivo*; this failure was observed as early as division 1 (Fig. 1d, e and Extended Data Fig. 1 c, e). This was in sharp contrast to E-TCR_{TAG} from livers or spleens of infected mice, which produced effector cytokines (IFNγ/TNF) and cytolytic molecules (GZMB/PRF1) and were capable of degranulation (CD107a membrane localization) within a few cell divisions (Fig. 1d, e and Extended Data Fig. 1c, d, e). Thus, tumor antigen encounter drove CD8 T cell activation and proliferation without gain of effector function.

TST effector function impairment begins before cell division

Given that TST effector function impairment was apparent within a few cell divisions, we next assessed differentiation following activation prior to cell division (6h, 12h, 18h) (Fig. 2a). T-TCR_{TAG} were activated within 6h with similar kinetics as in infected mice, evidenced by CD69 induction and up-regulation of CD44, LAG3, and PD1 (Fig. 2b and Extended Data Fig. 2a). While E-TCR_{TAG} produced effector cytokines at these early time points, T-TCR_{TAG} showed loss of TNF and failure to induce IFNγ within 6h, with near total failure to produce

both cytokines by 12h (Fig. 2c, d and Extended Data Fig. 2c). T-TCR_{TAG} also failed to produce GZMB (Fig. 2d and Extended Data Fig. 2b). Thus, multiple arms of effector function were impaired in TST within hours of activation as compared to infection-activated T cells. Interestingly, TOX, a DNA-binding protein shown to be associated with dysfunction in tumors and exhaustion in chronic viral infection[16, 17] was not induced at these early time points (Fig. 2e), confirming that TOX does not mediate effector function impairment as previously shown[17].

Effector CD8 T cells rapidly lose function in tumors

To rule out the possibility that rapid dysfunction in tumors is due solely to inadequate priming, we tested whether committed effector T cells would succumb to tumor-induced dysfunction with kinetics similar to naive T cells. We adoptively transferred CFSE-labeled day 5 effector TCR_{TAG} (E5d) from LM_{TAG}-infected B6 into tumor bearing ASTxAlb-Cre (E→T) or time matched LM_{TAG} infected B6 (E→E) and analyzed 12h, 36h, and 7 days (d) later (Fig. 3a). E→E re-expressed CD127 (IL7R) (Fig. 3b) and remained IFNγ/TNF double producers in the liver (Fig. 3c, d) and spleen of secondary recipients (Extended Data Fig. 3a, b), demonstrating that E5d were committed functional effectors that underwent memory differentiation and were not negatively impacted by trafficking to the liver microenvironment. In contrast, E→T proliferated after transfer but began losing cytokine production capacity within 12h, with complete loss by 7d (Fig. 3b, c, d). E→T exhibited the classical hierarchical progression of dysfunction/exhaustion[20], with loss of TNF first, followed by IFNγ (Fig. 3c and Extended Data Fig. 3c). Remarkably, nearly all the effector function loss occurred prior to cell division (Extended Data Fig. 3c, d), demonstrating again that cell division is not needed to disable effector function.

TST dysfunction kinetics in mice with metastatic melanoma

To test whether the rapid loss of TST effector function occurred in other cancer types/tissues with distinct antigen specificity, we utilized a pulmonary melanoma metastasis model. Metastases were induced in B6 mice through i.v. injection of B16 murine melanoma cells expressing the CD8 T cell-recognized $ovalbumin_{257\text{-}264}$ epitope fused to EGFP (B16-OVA). Naive OVA-specific TCR transgenic CD8 T cells (TCR_{OTI}) were adoptively transferred into B16-OVA-bearing or LM_{OVA}-infected B6 and analyzed 16h and 48h later (Fig. 4a). T-TCR_{OTI} and E-TCR_{OTI} were rapidly activated as evidenced by CD69 and PD1 induction prior to first cell division (Extended Data Fig. 4a, b). At 48h, both T-TCR_{OTI} and E-TCR_{OTI} proliferated robustly and upregulated CD44 and LAG3 (Fig. 4b). Despite proliferating, T-TCR_{OTI} failed to make TNF and IFNγ (Fig 4c, d) and only produced minimal GZMB (Fig. 4d). In marked contrast, E-TCR_{OTI} produced TNF, IFNγ, and GZMB by 16h following activation and became more functional with time (Fig. 4c, d and Extended Data Fig. 4c).

We next tested whether committed OVA-specific effector T cells would lose function in hosts with pulmonary melanoma metastases. We adoptively transferred CFSE-labeled day 5 effector TCR_{OTI} (E5d) from LM_{OVA}-infected B6 and adoptively transferred them into time-matched LM_{OVA}-infected mice (E→E) or B6 with established pulmonary B16-OVA metastases (E→T) (Fig. 4e). Within 24h following transfer, when majority of the population had not yet divided (Extended Data Fig. 4d), E→T TCR_{OTI} began losing the ability to

produce TNF and IFNγ, in contrast to E→E TCR_{OTI}, which remained highly functional (Fig. 4f, g). These findings suggest that the rapid onset of TST dysfunction is not specific to the liver microenvironment or liver tumors but can occur in other advanced cancers in different tissues and with different tumor types and antigen specificities.

Dysfunction-associated epigenetic programs arise pre-division

Our finding of pre-division dysfunction in TST led us to ask whether dysfunction-associated epigenetic remodeling also occurred prior to cell division. We transferred CFSE-labeled TCR_{TAG} into tumor-bearing ASTxAlb-Cre or LM_{TAG}-infected B6, sorted pre-division T-TCR_{TAG} (from liver tumors at 6h, 12h, 24h) and E-TCR_{TAG} (from spleen at 6h, 12h, 24h), and assessed chromatin accessibility by Assay for Transposase-Accessible Chromatin with sequencing (ATAC-SEQ)[21] and gene expression by RNA-Sequencing (RNA-SEQ) (Fig. 5a and Extended Data Fig. 5a). Principle component analysis (PCA) of ATAC-SEQ and RNA-SEQ data showed that within 6h, T- and E-TCR_{TAG} had distinct chromatin accessibility and gene expression profiles (Fig. 5b and Extended Data Fig. 5b). Strikingly, the largest number of chromatin remodeling changes occurred during the first 6h post-activation, with fewer changes occurring at 12 and 24h (Fig. 5b, c). 64% of differentially accessible chromatin peaks (DAC) were shared between E- and T-TCR_{TAG} (Fig. 5d) and included TCR signaling downstream genes (*Irf4*, *Nfatc2*, *Nfkb1*, *Lat*). Notably, a large number of peaks were more differentially accessible in T-TCR_{TAG} as compared to E-TCR_{TAG} (21%) (Fig. 5d). *Pdcd1* contains an enhancer peak 23 kb upstream from the transcription start site (−23 kb) previously shown to be preferentially opened in later dysfunctional/exhausted T cells in tumors[5] and during chronic viral infection[22, 23, 24]. Remarkably, we found that the −23kb "exhaustion"-associated *Pdcd1* peak was more accessible within 6h of T cell activation in tumors (Extended Data Fig. 5c). To identify potential TF driving early chromatin remodeling differences, we used ChromVar[25] to perform motif analysis on DAC between E6-24h and T6-24h. Motifs associated with inflammatory cytokine-induced TF such as STAT family members were preferentially enriched in early E-TCR_{TAG} DAC (Fig. 5e), consistent with *Listeria*-induced innate immune activation[26, 27]. When we examined expression by RNA-SEQ, there were more differentially-expressed genes (DEG) with peaks containing STAT1 motifs in E-TCR_{TAG} compared to T-TCR_{TAG}, and gene expression changes mainly correlated with the direction of the peak change (Extended Data Fig 6a). Upregulated genes containing STAT1 motif peaks encoded cytokine receptors, such as *Il12rb,* and inflammation-associated genes such as *Oasl1*[28]. On the other hand, in TST, NFAT TF family motifs were enriched in DAC (Fig. 5e). We previously showed that NFAT drives expression of multiple inhibitory receptors[5] as well as TF TOX[17] in TST at later time points. Thus, alterations in NFAT activity in TST begin within hours of activation and may result from NFAT association with different TF partners or genomic locations[29] as compared to T cells in acute infection.

Gene set enrichment analysis (GSEA) showed that early activated TCR_{TAG} in infected mice and tumor-bearing mice as compared to naive TCR_{TAG} shared enrichment for genes associated with T cell activation (Extended Data Fig. 6b). T-TCR_{TAG} and E-TCR_{TAG} also shared enrichment for gene sets associated with purine/pyrimidine metabolism, MYC targets, translation, glycolysis, and oxidative phosphorylation, known to be induced post-

TCR activation[30] (Extended Data Fig. 6b). When we compared T-TCR_{TAG} and E-TCR_{TAG} head-to-head, we found that early E-TCR_{TAG} were enriched for gene sets associated with IFNα and IFNγ responses (Fig. 5f), consistent with STAT TF motif enrichment in DAC (Fig. 5e). In contrast, early T-TCR_{TAG} were enriched for gene sets expressed in T cells stimulated in the absence of signal 3/inflammation (Fig. 5f). These analyses suggest that T cells activated in infected and tumor-bearing hosts received similar TCR stimulation, however T cells activated in tumor-bearing hosts failed to receive inflammatory cytokine signaling present in infected hosts.

We next asked how pre-division infection and tumor-activated TCR_{TAG} transcriptional profiles compared with T cell profiles at later time points. Early E-TCR_{TAG} showed enrichment for gene sets associated with later effector (day 6) and memory T cells (day 30) from acute infection (Fig. 5f). In contrast, early T-TCR_{TAG} showed enrichment for gene sets associated with later dysfunctional/exhausted T cells in tumors (day 5-30) or chronic viral infection (day 30) (Fig. 5f). In line with these findings, T-TCR_{TAG} induced greater expression of negative regulators of T cell function (*Rgs16*, *Pdcd1*, *Ptpn22*), and lower expression of inflammation-associated genes (*Mx1*, *Isg15*), genes encoding cytokines/cytolytic mediators (*Ifng*, *Gzmb*, *Gzma*), and genes encoding TF associated with functional differentiation (*Batf*, *Tbx21*)[31] (Fig. 5g). T-TCR_{TAG} expressed more *Bach2* and *Id3*, previously associated with memory phenotypes[32] and restraint of effector differentiation (Fig. 5g)[33]. Taken together, our data demonstrate that epigenetic and transcriptional changes previously associated with late-stage dysfunctional/exhausted T cells are already induced within hours of activation in tumor-bearing hosts.

Chromatin remodeling is reinforced with time/tumor antigen

We next asked whether pre-division dysfunction-associated chromatin accessibility changes are maintained or evolve with time and continued antigen exposure. We compared chromatin accessibility in T6h-T24h with our previously published chromatin accessibility data in TCR_{TAG} isolated from liver tumors after 5-60d[5]. We also carried out ATAC-SEQ on TCR_{TAG} sorted from ASTxAlb-Cre after 5d (T5d) and 10d (T10d). PCA showed that TST chromatin accessibility clustered into three groups based on the duration of tumor exposure: early (6-24h), intermediate (5-10d), and late (14-60+d) (Fig. 6a). T5d from malignant liver lesions (ASTxAlb-Cre; 2023) had similar chromatin accessibility profiles as T5d isolated from pre-malignant liver lesions (ASTxCre^{ERT2}; 2017) (Fig. 6a). The greatest number of TST chromatin peak changes (DAC) occurred within 6h, with another large round of changes between 24h-5d, and a third smaller round between 7-14d, after which there was little chromatin remodeling (Fig. 6b right, Extended Data Fig. 7a). TCR_{TAG} in the setting of acute infection also had many early peak changes within 6h and a second round of peak changes between 24h and 5d; however, in contrast to TST in tumors that underwent a third wave of chromatin remodeling, likely driven by continued tumor antigen exposure, few peak changes occurred after E5d (Fig. 6b **left**, Extended Data Fig. 7a, b), demonstrating that the memory-associated chromatin state was largely established early by day 5 upon pathogen/antigen clearance.

We next compared how individual chromatin peaks (DAC) changed over time by plotting the fold-change of each peak's accessibility during the early transition (naive (N) to 6h) versus during the intermediate (int) transition, (24h to 5d) (Fig. 6c, d). Thus, a peak in the "reinforced open" quadrant in the scheme in Fig. 6c had an increase in accessibility between N and 6h with a further increase in accessibility between 24h and 5d. In contrast, a peak in the "stable closed" quadrant had an early decrease in accessibility and remained "closed" during the later transition. This analysis revealed that 36% of pre-division remodeled chromatin peaks in TST remained stable (19% closed, 17% open) with continued tumor/antigen exposure, with additional peaks reinforced with time (13%) or opening at the intermediate transition (int, 16%) (Fig. 6d **lower**). Thus, nearly 50% (stable + reinforced) of the T5d chromatin accessibility signature was already established within the first 6 hours after activation in tumors. This was in marked contrast with differentiation during infection, in which many early DAC were transient (51%) or newly occurring between 24h and 5d (int 19%) (Fig. 6d **upper**). While tumor and infection activated T cells underwent some chromatin remodeling during the intermediate to late (T14d or M) transition, most chromatin accessibility changes (>60%) remained stable (Extended Data Fig. 7c). The *Pdcd1* locus exemplifies these patterns, with peak changes maintained and reinforced with time in tumors and transient during acute infection-induced effector/memory differentiation (Fig. 6e, f), consistent with PD1 surface expression (Extended Data Fig. 1a). The dysfunction/exhausted-associated −23kb *Pdcd1* enhancer peak opened early only in tumors and was reinforced at later time points, while the peak at +4.5kb, transiently opened during infection, remained stably opened in tumors, and the peak at +10kb opened only at the intermediate time point (int open) in tumors (Fig. 6e).

To identify potential TF driving specific transitional peak changes during effector and TST differentiation, we carried out Motif aNAlysis with Lisa (monaLisa)[34]. While TF enrichment in the transiently opened peaks (light purple) was overall similar between E- and T-TCR_{TAG}, NFAT TF family motifs were particularly enriched in peaks with reinforced (light orange) and later/intermediate (dark orange) opening in tumors but not during infection (Fig. 6g), consistent with TCR_{TAG} receiving continuous antigen/TCR stimulation in tumors but only transient stimulation during acute infection. In contrast, T-box TF family motifs, including those of TBET (TBX21) and EOMES, were more enriched in peaks that opened early and were predominantly reinforced (light orange) during infection, but less so in tumors (Fig. 6g), consistent with the role of these TF in facilitating functional effector formation during acute infection and functional memory populations following pathogen/antigen clearance[35, 36, 37, 38].

Tumor exposure duration determines dysfunction imprinting

Given the observation that many chromatin accessibility changes in TCR_{TAG} were stabilized and/or reinforced with increased tumor/antigen exposure, we next asked if TCR_{TAG} removed from tumors and transferred to tumor-free hosts would retain the functional, immunophenotypic, and epigenetic hallmarks of dysfunction. TCR_{TAG} were re-isolated from liver tumors after 1, 5, or 10 days (T24h, T5d, and T10d) and parked in tumor-free B6 mice (P24h, P5d, P10d) for 5 days (Fig. 7a). In parallel with functional and immunophenotypic analysis, we carried out ATAC-SEQ on the pre- and post-parking samples. Prior to transfer,

tumor-activated TCR_{TAG} failed to make cytokine (Fig. 7b). After 5 days of parking, P24h had uniformly downregulated PD1 (Fig. 7c), yet 35-40% remained unable to produce TNF or IFNγ (Fig. 7b, d). With longer tumor exposure, more TCR_{TAG} had "imprinted" effector function loss, with nearly all P10d failing to make effector cytokine and retaining PD1 expression (Fig. 7b, c).

Heterogeneity has been described for dysfunctional/exhausted T cells, with more stem-like TCF1+ dysfunctional/exhausted T cells needed to sustain anti-viral/anti-tumor effects[39, 40, 41, 42] and reviewed in[43]. To determine whether such heterogeneity explained the partial recovery of effector function observed in P24h and P5d, we examined TCR_{TAG} expression of stem/progenitor v terminal differentiation markers at early, intermediate, and late time points (Extended Data Fig. 8a). At 36h post-transfer into ASTxAlb-Cre, undivided and early division TCR_{TAG} in the livers and spleens of ASTxAlb-Cre uniformly expressed TCF1 at the same or higher level as naive TCR_{TAG} (Extended Data Fig. 8b). In contrast, T60+d in the liver had markedly downregulated TCF1 (Extended Data Fig. 8b). To look for evidence of bimodal stem/progenitor versus terminally-differentiated populations, we examined concurrent expression of CD38 and CD101, surface markers correlated with a terminally-differentiated dysfunctional state and loss of reprogrammability[5]. T36h and T5d remained low for both CD38 and CD101, in contrast to T60+d, which were CD38+ and heterogeneous for CD101 (Extended Data Fig. 8c). T36h and T5d also showed homogeneous expression of TCF1 and TOX, becoming $TCF1^{low}$ and TOX^{high} only at later time points (T60+d) (Extended Data Fig. 8c). Thus, the dichotomous marker expression previously associated with stem/progenitor and terminally-differentiated exhausted T cells does not clearly correlate with the ability of early TST to recover cytokine function after parking. We cannot exclude the possibility that smaller, more graded expression changes at the individual cell level may regulate or predict cytokine recovery.

When we assessed chromatin accessibility, we found that the post-parking samples clustered separately from pre-parking samples or from antigen-experienced memory T cells (Fig. 7e, f). We used a similar scatterplot analysis as described in Fig. 6c to characterize peak changes (DAC) pre- and post-parking. Many peak changes in T24h were transient, reverting after 5d parking in tumor-free hosts, and there were fewer stable peaks (Fig. 7g). However, with longer tumor exposure, the number of transient peaks decreased while the number of stable peaks increased (Fig. 7g). Correspondingly, chromatin accessibility at the *Pdcd1* −23kb enhancer in post-parking TCR_{TAG} increased with longer tumor exposure (Extended Data Fig. 9a). In contrast, TOX expression was uniformly lost after TCR_{TAG} removal from tumor, even after 10d of tumor exposure, (Fig. 7c, d), suggesting that TOX expression is dependent on continued antigen/TCR stimulation and/or requires even longer tumor exposure to become imprinted. Recent studies showed that later exhausted T cells (>30d exposure) from humans and murine models of chronic viral infection retain TOX expression together with exhaustion-associated chromatin peaks ("epigenetic scarring") after transfer to antigen-free hosts or viral cure with direct acting anti-viral therapy[44, 45, 46]. While we observed evidence of "epigenetic scarring" in some *Tox* locus peaks, other peaks, particularly peaks that appeared during the intermediate and late time points, were not retained in post-parking TCR_{TAG} (Extended Data Fig. 9b).

To identify the drivers of progressive imprinting of dysfunction hallmarks, we asked how TF motif enrichment changed in pre- and post-parking DAC. Open chromatin peaks in post-parking TCR_{TAG} showed enrichment for CTCF motifs (Fig. 7h), intriguing in light of recent studies showing that CTCF-mediated genome reorganization promotes CD8 T effector differentiation[47]. NFAT TF family enrichment, which increased in intermediate TCR_{TAG}, was lost upon removal from tumors (Fig. 7h), suggesting that NFAT-mediated DAC are maintained by continued TCR signaling. Post-parking samples clustered closer to memory TCR_{TAG} than did pre-parking samples (Fig. 7e,f), possibly reflecting the fact that post-parking and memory TCR_{TAG} are not undergoing antigen/TCR stimulation. However, memory TCR_{TAG} produce high levels of TNF and IFNγ upon antigen restimulation (Fig. 3 and [5, 15]), whereas the post-parking TCR_{TAG} largely failed to do so (Fig. 7b). We used HOMER[48] to compare TF motif enrichment in chromatin peaks in P5d and M and found that KLF family motifs were predominant in non-functional post-parking TCR_{TAG} peaks (Fig. 7i), consistent with previously described roles in T cell quiescence, functional restraint, and fixed dysfunction[5, 49, 50]. In contrast, memory TCR_{TAG} showed enrichment for memory-associated TCF1 and ZEB family[51, 52, 53] family motifs, lacking in P5d (Fig. 7i). Interestingly, the *Ifng* locus contained a peak uniquely accessible in memory TCR_{TAG} (+14kb) that was not present in pre- and post-parking tumor samples (Extended Data Fig. 9c). This peak was previously shown to be accessible in functional NK cells and to bind TBET[54]. In contrast, a peak in *Ifng* at +19kb was not present in memory TCR_{TAG} but present in both pre- and -post parking TST. Thus, removing T cells from tumor at early and intermediate time points may reverse TCR-driven inhibitory signals and some dysfunction-associated chromatin remodeling, however, effector function is not recovered because T cells activated in tumors have failed to induce function/memory-defining TF.

DISCUSSION

Here, we describe for the first time the functional, immunophenotypic, epigenetic, and transcriptional features of TST differentiation within the hours following tumor antigen encounter *in vivo*. Though TST were activated and proliferated similarly to CD8 T cells during acute infection, TST in tumor-bearing hosts failed to gain both effector cytokine and cytolytic function. Remarkably, this dysfunction was evident even prior to cell division. Rapid effector function impairment *in vivo* coincided with extensive chromatin remodeling and transcriptional alterations in TST within 6 hours post tumor antigen encounter, including hallmark chromatin accessibility changes previously characterized as “exhaustion-associated.” These findings upend the paradigm that tumor-induced T cell dysfunction requires chronic antigen stimulation over days to weeks and instead show that CD8 T cell integrate multiple signaling inputs (TCR, co-stimulatory/inhibitory, and cytokine) immediately following activation in different contexts, which dictate their epigenetically encoded differentiation to the functional effector state (infection) or to the dysfunctional state (tumors).

Proliferation and differentiation are intimately connected throughout development[6], and previous studies showed that proliferation was required for the epigenetic remodeling associated with differentiation for thymocytes and other adaptive immune lineages[7, 8, 9, 10]. However, we find that CD8 T cells execute large scale chromatin remodeling and

differentiation prior to undergoing cell division. As our study is the first to examine adaptive immune cell differentiation and chromatin remodeling during the first hours following activation *in vivo* prior to cell division, it remains to be seen whether other immune cells similarly undergo early rapid differentiation to the functional or dysfunctional state. Nevertheless, despite losing effector function, dysfunctional TST proliferated rapidly and robustly; thus, the regulation of proliferation and functional effector differentiation is uncoupled. This finding, in line with previous studies *in vitro* or in self-tolerance models[55, 56, 57] has important implications for cancer immunotherapy, as efforts aimed at boosting TST proliferation by gene targeting may not be sufficient to reverse effector function loss[58, 59, 60].

While dysfunctional hallmarks, including impaired effector function, inhibitory receptor expression, and dysfunction/exhaustion-associated chromatin accessibility changes, were manifested in TST with different kinetics prior to cell division, with continued tumor/antigen stimulation and proliferation, TST underwent additional chromatin remodeling that stabilized and reinforced initial dysfunction epigenetic programs. These findings together with our previous work[5, 17] demonstrate that the T cell dysfunctional state is composed of different modules (loss of effector function, upregulation of inhibitory receptors, proliferative capacity), which are regulated independently. This was borne out when we tested the degree to which early TST dysfunction was “imprinted”—that is retained upon removal from the tumor and transfer into tumor-free hosts. Effector function impairment was not reversed upon tumor removal in a significant fraction of TST exposed to tumor for 24h, in contrast to PD1 expression, which was nearly absent in P24h and did not become fixed until after 5+ days of tumor exposure, with epigenetic reinforcement.

The heterogeneity in effector function recovery observed upon early TST removal to tumor-free hosts raised the question as to whether there was bifurcation in early/intermediate time point populations towards stem/progenitor or terminally-differentiated dysfunctional/exhausted states. However, in contrast to studies in chronic LCMV infection models[61], we found that early/intermediate TST had homogeneous expression of TCF1 and did not express late/terminal exhaustion/dysfunction markers. While TST dysfunction shares many features with the chronic viral infection-induced exhaustion, there are important biological differences between hosts with late-stage tumors and hosts with chronic infection that may be particularly relevant during the initial hours and days immediately following activation. Early time point TST did not show induction of inflammation-associated TF or downstream inflammation-associated genes, and this lack of innate/inflammatory cytokine stimulation may lead to the failure of TST to induce functional/memory-associated gene programs, even upon removal from tumor. In contrast, chronic viral infection does induce innate immune signaling, and indeed, CD8 T cells activated during acute and chronic viral infection have comparable effector function, with loss of cytokine and cytolytic function occurring over days to weeks[62].

Taken together, our studies suggest that there are two major contributing factors to TST dysfunction in hosts with late-stage tumors. First, TST activated in tumors or secondary lymphoid organs may receive strong TCR signaling due to a surfeit of tumor antigen, leading to robust activation and proliferation; however, the lack of innate inflammatory

signals in tumors leads to a failure to induce TF regulating functional effector differentiation. Second, persistent tumor antigen/TCR stimulation and/or other negative regulatory signals in tumor-bearing hosts leads to ongoing NFAT activity or partnerless NFAT activity, further impairing effector function and inducing TOX expression as well as multiple other negative regulators of T cell signaling and function. In addition, chronic tumor antigen/TCR stimulation reinforces epigenetic programs encoding dysfunctional hallmarks, eventually leading to fixed dysfunctional TST.

The rapid loss of function in committed effector CD8 T cells upon transfer into mice with late-stage liver and pulmonary melanoma metastases was particularly striking, demonstrating that the negative regulatory factors in hosts with advanced tumors can overwrite functional epigenetic programs in CD8 T cells. Thus, even T cells that have been optimally activated in tumor-bearing hosts (e.g. through immunization or by activated antigen presenting cells in draining lymph nodes), may still succumb to tumor-induced dysfunction upon entry into tumors. These findings have important implications for immunotherapies such as adoptive T cell therapies and immune checkpoint blockade.

Given how rapidly CD8 T cells acquire dysfunctional hallmarks in tumor-bearing hosts, with early epigenetic remodeling further reinforced over time/tumor progression, we need to target both early dysfunction induction as well as dysfunction reinforcement in order to improve T cell-based cancer immunotherapy. Further studies are needed to understand how CD8 T cells rapidly integrate TCR and context-dependent inputs to make fate choices. By deciphering the complex network of signaling and gene regulatory networks driven by TCR and context-dependent inputs, we can design better strategies to alter or redirect T cells into functional cancer killers.

METHODS

Mice.

TCR_{TAG} transgenic mice (B6.Cg-Tg(TcraY1,TcrbY1)416Tev/J)[63], TCR-OT1 (C57BL/6-Tg(TcraTcrb)1100Mjb/J), Ly5.1 (B6.SJL-Ptprca Pepcb/BoyJ), Alb-Cre (B6.Cg-Tg(Alb-cre)21Mgn/J), and C57BL/6J Thy1.1 mice were purchased from The Jackson Laboratory. TCR_{TAG};Thy1.1 double transgenic mice were generated by crossing Thy1.1 mice to TCR_{TAG} mice. TCR_{OVA};Ly5.1 double transgenic mice were generated by crossing the TCR-OTI mice with Ly5.1 mice. ASTxAlb-Cre[15] double transgenic mice were generated by crossing AST (Albumin-floxStop-SV40 large T antigen (TAG))[64] with Alb-Cre mice. ASTxAlb-Cre were used between 9-12 weeks of age, at which time all mice had established liver tumors. Both female and male mice were used for studies. T cell donor mice were between 6-10 weeks of age and sex-matched to recipient male and female C57BL/6 and ASTxAlb-Cre recipients. All mice were bred and housed in the animal facility at Vanderbilt University Medical Center (VUMC). Mice were on 12h light-dark cycles. The mouse housing facility was maintained at 20-25C and 30-70% humidity. All animal experiments were performed in compliance with VUMC Institutional Animal Care and Use Committee (IACUC) regulations and in accordance with approved VUMC IACUC protocol M1700166-01.

Adoptive T cell transfer in acute infection and tumor models.

C57BL/6 mice were inoculated i.v. with $5x10^6$ or $10x10^6$ CFU *Listeria monocytogenes* (LM) Δ*actA* Δ*inlB* strain[65] expressing the TAG-I epitope (SAINNYAQKL, SV40 large T antigen 206–215) (Aduro Biotech) or the OVA epitope (SIINFEKL), respectively, 6-12h prior to T cell adoptive transfer for generation of effectors. Spleens from naive TCR_{TAG};Thy1.1 mice were mechanically disrupted with the back of 3 mL syringe and filtered through a 70 μm strainer into ammonium chloride potassium (ACK) buffer to lyse erythrocytes. Cells were washed twice with cold serum-free RPMI 1640 media and $2.5x10^6$ TCR_{TAG};Thy1.1 $CD8^+$ T cells were adoptively transferred into C57BL/6 (Thy1.2) mice inoculated with LM_{TAG} or ASTxAlb-Cre tumor bearing mice. For OTI experiments $2.5x10^6$ TCR_{OVA};Ly5.1 splenocytes were prepared in the same manner from OTI;Ly5.1 mice and adoptively transferred into mice inoculated with LM_{OVA} or mice bearing B16-OVA lung tumors. For CFSE labeling studies, splenocytes were resuspended after first wash in 2.5 mL of plain, serum-free RPMI 1640, rapidly mixed with equal volumes of 2x CFSE [10μM] solution, incubated for 5 min at 37°C at a final CFSE [5 μM], quenched by mixing CFSE/cell solution with equal volume of pure FBS, washed twice with serum-free RPMI, and resuspended in serum-free RPMI for transfer.

B16-OVA Production and Lung Metastasis.

B16-F10 mouse melanoma cell line was obtained from ATCC (CRL-6475). B16-OVA expressing cell line was produced by transduction with pMFG-OVAx2-EGFP overexpression vector. Briefly, pMFG-EGFP was linearized with NcoI and ligated with OVAx2 (SIINFEKL-AAY-SIINFEKL) containing oligonucleotide (IDT). Cloned constructs were sequence verified. Phoenix-AMPHO (ATCC, CRL-3213) packaging cells were transfected with pMFG-OVAx2-EGFP in calcium phosphate and B16-F10 was transduced with viral supernatant. B16-OVA cells were sorted by EGFP expression for freeze downs and culturing. B16-OVA were cultured in Dulbecco's Modified Eagle's Medium (DMEM) supplemented with 10% FBS and L-Glutamine (cDMEM) at 37C in a 5% CO2 humidified incubator. For inoculation of lung metastasis, B16-OVA was harvested at 60-80% confluency. Media was replaced with fresh cDMEM the day prior to harvest. Cells were washed twice with ice cold serum free RPMI and $2\text{-}4x10^5$ cells were injected by tail vein into B6 mice. Tumors were allowed to grow for 3 weeks prior to T cell transfer experiments. The maximal tumor size permitted for transplantable tumors as per our VUMC IACUC-approved protocol is 3 cm in maximum diameter. No tumors in this study exceeded the maximal allowed tumor size.

Cell isolation for subsequent analyses.

Spleens from experimental mice were mechanically disrupted with the back of 3 mL syringe and filtered through a 70 μm strainer into ACK buffer. Cells were washed once and resuspended in cold RPMI 1640 supplemented with 2μM glutamine, 100U/mL penicillin/streptomycin, and 10% FBS (cRPMI). Liver tissue was mechanically disrupted using a 150 μm metal mesh and glass pestle in ice-cold 2% FBS/PBS and passed through a 70 μm strainer. Liver homogenate was centrifuged at 400g for 5 min at 4°C and supernatant discarded. Liver pellet was resuspended in 20 mL of 2% FBS/PBS buffer containing 500

U heparin, mixed with 13 mL of Percoll (GE) by inversion, and centrifuged at 500g for 10 min at 4°C. Supernatant was discarded and pellet was RBC lysed in ACK buffer and resuspended in cRPMI for downstream applications. Periportal and celiac lymph nodes were collected and pooled for tumor draining lymph node analysis. Lymph nodes were mechanically dissociated into single cell solutions using the textured surface of two frosted microscope slides into ice-cold cRPMI.

Intracellular cytokine staining and transcription factor staining.

Intracellular cytokine staining was performed with the Foxp3/Transcription Factor Staining Buffer Kit (Tonbo) per manufacturer's instructions. Briefly, T cells were mixed with $2x10^6$ C57BL/6 splenocytes and stimulated with 0.5 μg/mL of TAG epitope I peptide in cRPMI for 4 hours at 37°C in the presence of brefeldin A (BioLegend). Where indicated, stimulation media contained anti-CD107a antibody. Following peptide stimulation, cells were stained with for surface markers, fixed, permeabilized, and stained for IFNγ, TNF, perforin, and granzyme B. Intracellular transcription factor staining was performed with the Foxp3/Transcription Factor Staining Buffer Kit (Tonbo) per manufacturer's instructions

Flow cytometry and flow sorting.

All flow analysis was performed on the Attune NXT Acoustic Focusing Cytometer (ThermoFisher Scientific). The following fluorochrome-conjugated antibodies were used in analysis. Clone is denoted in parentheses.

Anti-CD8-BV605 (53-6.7), BioLegend, Cat# 100744, Lot# B318405, Dilution 1:250

Anti-CD8-PE (53-6.7), Tonbo, Cat# 50-0081-U100, Lot# C0081013017503, Dilution 1:800

Anti-CD44-PCP-Cy5.5 (IM7), Tonbo, Cat# 65-0441-U100, Lot# C0441070121653, Dilution 1:200

Anti-CD44-FITC (IM7), BioLegend, Cat# 103006, Lot# B228504, Dilution 1:200

Anti-CD44-APC (IM7), Tonbo, Cat# 20-0441-U100, Lot# C0441022119203, Dilution 1:200

Anti-CD44-AF700 (IM7), eBioscience, Cat# 56-0441-80, Lot# 1995539, Dilution 1:200

Anti-CD62L-BV785 (MEL-14), BioLegend, Cat# 104440, Lot# B340191, Dilution 1:200

Anti-CD69-PE-Cy7 (H1.2F3), eBioscience, Cat# 25-0691-82, Lot# 1981586, Dilution 1:200

Anti-CD90.1-BV421 (OX-7), BioLegend, Cat# 202529, Lot# B305864, Dilution 1:1000

Anti-CD90.1-PCP-Cy5.5 (HIS51), eBioscience, Cat# 45-0900-80, Lot# 2227596 Dilution 1:800

Anti-CD90.1-APC (HIS51), eBioscience, Cat# 17-0900-82, Lot# 2162254, Dilution 1:800

Anti-CD90.1-APC-eF780 (HIS51), eBioscience, Cat# 17-0900-82, Lot# 2142928, Dilution 1:800

Anti-CD127-FITC (A7R34), BioLegend, Cat# 135007, Lot# B255262, Dilution 1:200

Anti-CD107a/LAMP1-FITC (ID4B), BioLegend, Cat# 121606, Lot# B283798, Dilution 1:400

Anti-GZMB-PE-Cy7 (GB11), BioLegend, Cat# 372214, Lot# 2361830, Dilution 1:200

Anti-GZMB-AF647 (GB11), BioLegend, Cat# 515406, Lot# B341642, Dilution 1:200

Anti-IFNgamma-BV421 (XMG1.2), BioLegend, Cat# 505829, Lot# B335329, Dilution 1:400

Anti-IFNgamma-PE-Cy7 (XMG1.2), BioLegend, Cat# 505825, Lot# B334480, Dilution 1:1000

Anti-IFNgamma-APC (XMG.12), BioLegend, Cat# 505810, Lot# B290393, Dilution 1:800

Anti-LAG3/CD223-PE (eBioC9B7W), BioLegend, Cat# 12-2231-83, Lot# 2229141, Dilution 1:200

Anti-PD1/CD279-PCP-eF710 (RMP1-30), eBioscience, Cat# 46-9981-80, Lot# 2294181, Dilution 1:200

Anti-PD1/CD279-APC (RMP1-30), BioLegend, Cat# 109112, Lot# B309096, Dilution 1:200

Anti-TCF1-AF647 (C63D9), Cell Signaling Technology, Cat# 6709S, Lot# 12, Dilution 1:400

Anti-TNFalpha-PE (MP6-XT22), Life, Cat# 12-7321-82, Lot# 2124591, Dilution 1:600

Anti-TOX-PE (REA473), Miltenyl Biotec, Cat# 130-120-716, Lot# 5220109273, Dilution 1:200

The following fluorescent cell dyes were used in analysis.

CFSE, Tonbo, Cat# 13-0850, Lot# D0850042721, 5 uM

DAPI, BioLegend, Cat# 422801, Lot# B234813, 50 ng/mL

Ghost Dye Violet 450 Viability Dye, Tonbo, Cat# 13-0863-T500, Lot# D0868083018133, Dilution 1:1000

Ghost Dye Red 780 Viability Dye, Tonbo, Cat# 13-0865-T500, Lot# D0871072021133, Dilution 1:2000

Data was analyzed using FlowJo v.10.8.1 (Tree Star Inc.). Cell sorting was performed using the BD FACS Aria III (BD Biosciences) at the VUMC Flow Cytometry Shared Resource Core with BD FACSDiva Software. For pre- and post-parking analyses, target populations were enriched from spleens or malignant livers with CD8 negative selection kit Prior

to cell sorting workflows, (StemCell Technologies, Catalog # 19853) per manufacturer's instructions.

RNA sequencing (RNA-SEQ).

ACK lysed single cell suspensions from livers and spleens were processed as described above using sterile technique and stained with antibodies against CD8, CD90.1, and CD69 and (4',6-diamidino-2-phenylindole) DAPI for dead cell exclusion. 5,000 cells were sorted directly into Trizol LS and frozen. Total RNA was extracted from sorted cells using the Rneasy Micro kit (Qiagen) and amplified using the SMART-Seq v4 UltraLow Input RNA Kit (Clontech). The cDNA was quantified and analyzed on the BioAnalyzer. Libraries were prepared using 7.7-300 ng of cDNA and the NEB DNA Ultra II kit. Each library was quantitated post PCR and run on the Caliper GX to assess each library profile. A final quality control assay consisting of qPCR was completed for each sample. The libraries were sequenced using the NovaSeq 6000 with 150 bp paired end reads targeting 50M reads per sample. RTA (version 2.4.11; Illumina) was used for base calling and analysis was completed using MultiQC v1.7.5.

ATAC sequencing (ATAC-SEQ).

Profiling of chromatin was performed by ATAC-seq as previously described[25]. ACK lysed single cell suspensions from livers and spleens were processed as described above using sterile technique and stained with antibodies against CD8, CD90.1, and CD69 and (4',6-diamidino-2-phenylindole) DAPI for dead cell exclusion. 1,000-20,000 cells were sorted into cold FCS, DMSO added to 10%, and cells frozen. Frozen T cells were then thawed and washed in cold PBS and lysed. The transposition reaction was incubated at 42°C for 45 min. The DNA was cleaned with the MinElute PCR Purification Kit (Qiagen), and material was amplified for five cycles. After evaluation by real-time PCR, 7–13 additional PCR cycles were done. The final product was cleaned by AMPure XP beads (Beckman Coulter) at a 1× ratio, and size selection was performed at a 0.5× ratio. Libraries were sequenced on a HiSeq 2500 or HiSeq 4000 in a 50-bp/50-bp paired-end run using the TruSeq SBS Kit v4, HiSeq Rapid SBS Kit v2, or HiSeq 3000/4000 SBS Kit (Illumina).

Bioinformatics methods.

The quality of the sequenced reads was assessed with FastQC[66] and QoRTs[67] (for RNA-seq samples). Unless otherwise stated, plots involving high-throughput sequencing data were created using R v4.1.0[68] and ggplot2[69]. Code has been deposited in GitHub: https://github.com/abcwcm/Rudloff2022.

RNA-SEQ data analysis.

Adaptors were trimmed from raw sequencing reads with TrimGalore v0.5.0 (http://www.bioinformatics.babraham.ac.uk/projects/trim_galore/) and Cutadapt v2.8[70]. Trimmed reads were mapped with STAR v2.7.6a[71] to the mouse reference genome (GRCm38.p6). Fragments per gene were counted with featureCounts v2.0.7[72] with respect to Gencode vM25 comprehensive gene annotations. Differentially expressed genes were identified using

DESeq2 v1.34.0[73], and only Benjamini–Hochberg corrected *P* values (*FDR*) < 0.05 were considered statistically significant.

Gene set enrichment analysis was performed with fgsea v1.20.0[74], using genes ranked on the DESeq2 Wald statistic. KEGG, HALLMARK, and REACTOME gene sets were retrieved from the Broad Institute's MSigDB collections[75, 76] using msigbr v7.5.1[77]. Only pathways with an *FDR* value < 0.05 were considered enriched.

Principial component analysis and expression heatmaps were created using variance-stabilizing transformed counts generated by the DESeq2 package. Heatmaps are centered and scaled by row.

ATAC-SEQ data analysis

Alignment and identification of open chromatin regions: Reads were aligned to the mouse reference genome (GRCm38) with BWA-backtrack[78]. Post alignment filtering was done with samtools v1.8[79] and Broad Institute's Picard tools (http://broadinstitute.github.io/picard/) to remove unmapped reads, improperly paired reads, nonunique reads, and duplicates. To identify regions of open chromatin, peak calling was performed with MACS2 v2.2.7.1[80]. Only peaks with *FDR* values smaller than 0.01 were retained.

ATAC-SEQ peak atlas creation: A unified peak atlas was created from pre-division and post-parking samples, as well as from previously published chromatin accessibility data (GSE89308). Consensus peak sets were generated for each condition if a peak was found in at least 75% of replicates. These sets were then merged with DiffBind v3.4.11[81] to create an atlas of accessible peaks, which was used for downstream analyses. The peak atlas was annotated using the ChIPseeker v1.30.3[82] and Gencode vM25.

Differentially accessible regions: Regions where the chromatin accessibility changed between different conditions were identified with DESeq2 v1.34.0, and only Benjamini–Hochberg corrected *P* values (*FDR*) < 0.05 were considered statistically significant. A $\log_2$FC (cutoff of 1.5 was used in some analyses as indicated. Hidden batch effects were estimated using the svaseq function from sva v3.42.0[83], and the top 3 surrogate variables were accounted for in DESeq2.

Motif analysis: Peaks were analyzed for transcription factor (TF) motif enrichment using chromVAR v1.16.0[25]. Motifs from the CIS-BP database[84] ('mouse_pwms_v2' from chromVARmotifs v0.2.0) were used as input, after removing TFs that were lowly expressed based on the RNA-SEQ data (average count-per-million < 5). TF accessibility deviation scores and variability were calculated by chromVAR, and z-scores of deviations of the top 30 most variable TFs were visualized in a heatmap.

For identifying TF motifs enriched in differentially accessible peaks, we utilized HOMER via marge v0.0.4[48]. HOMER was run separately on hyper- or hypo-accessible peaks with the flags -size given and -mask. Motifs enriched in hyper- or hypo-accessible peaks were determined by comparing the rank differences (based on P value).

To compare TF motifs enriched in different peak classifications (transient, stable, reinforced, intermediate), we employed the calcBinnedMotifEnrR function from monaLisa v0.0.4[34]. The $\log_2$ enrichment was plotted in a heatmap if the motif was enriched in at least one category ($p < 1e\text{-}10$).

Peak heatmaps and genome coverage plots: Genome coverage files per replicate were normalized for differences in sequencing depth (RPGC normalization) with bamCoverage from deepTools v3.1.0[85]. Blacklisted regions were excluded (https://sites.google.com/site/anshulkundaje/projects/blacklists). Replicates were averaged together using UCSC-tools bigWigMerge and by dividing by the number of samples. ATAC-SEQ heatmaps were created using profileplyr v1.10.2[86] and ComplexHeatmap v2.15.1[87], by binning the region +/− 1kb around the peak summits in 20bp bins. To improve visibility, bins with read counts greater than the 75th percentile + 1.5*IQR were capped at that value.

Statistics and reproducibility.—No statistical method was used to predetermine sample size, but sample sizes are similar to those reported in previous publications[5, 15, 17]. No data were excluded from the analyses. The experiments were not randomized. The Investigators were not blinded to allocation during experiments and outcome assessment. Statistical analysis of NGS data is described in detail above. For all other experiments, statistical analysis, including two-tailed Student's T-test, two-way ANOVA with post hoc Tukey test, and one sample Student's t-test, were performed as described using Prism 9.0 software (GraphPad Software) and specified in figure legends. Data distribution was assumed to be normal but this was not formally tested. Composite figures and schematics were generated using Powerpoint 365 (Microsoft).

Extended Data

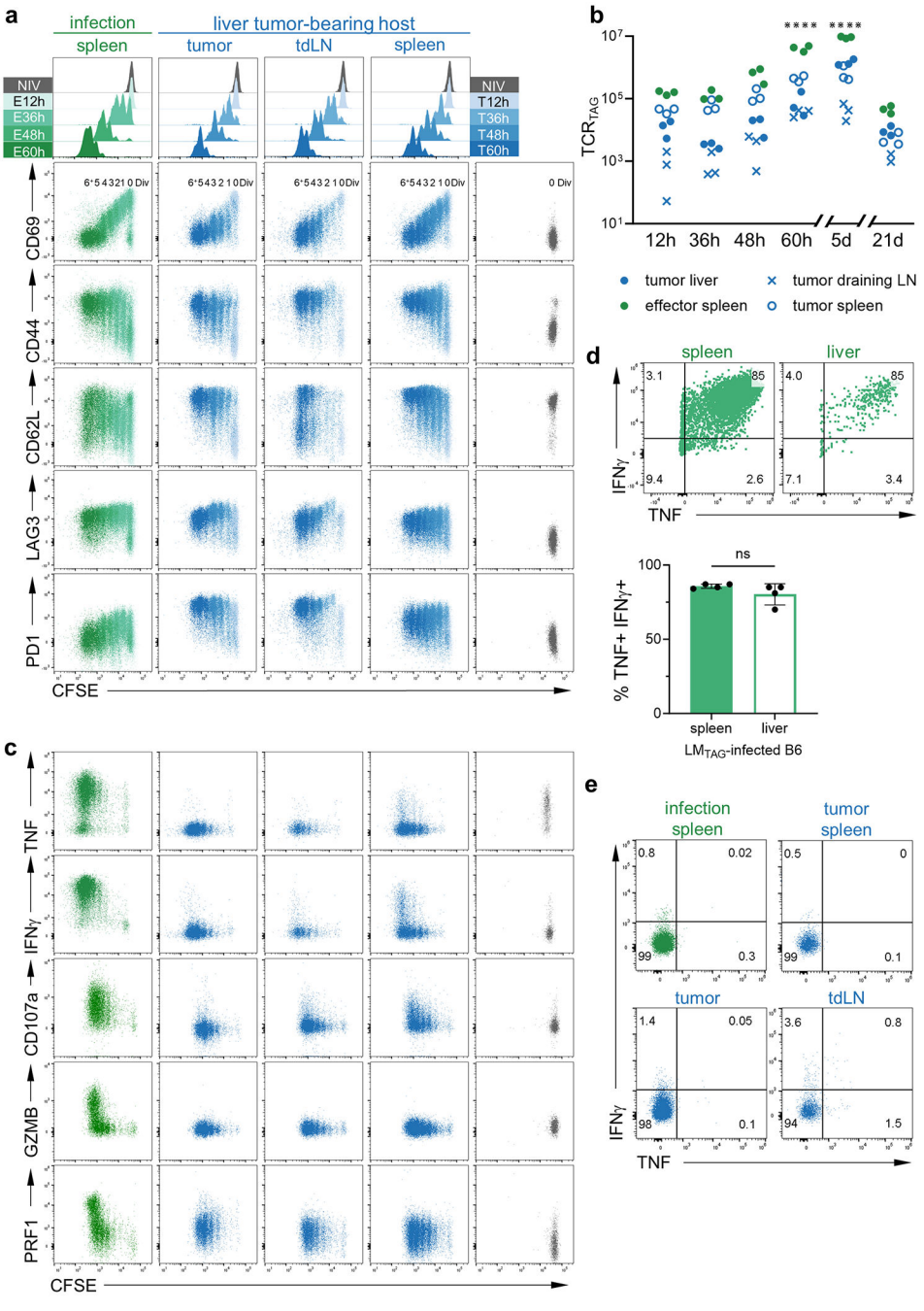

Extended Data Fig. 1. TST undergo robust activation and proliferation but do not gain effector function.

a, Live CD8$^+$ Thy1.1$^+$ TCR$_{TAG}$ CFSE dilution and expression of surface markers at each time point from LM$_{TAG}$-infected mice (spleens; green) or from tumor-bearing mice (blue), from liver tumors, tumor draining lymph nodes (tdLN), and spleens, shown together with naive *in vivo* control (N; grey). Each time point shows data concatenated from 3-4 biologic replicates. Three independent experiments were carried out with 3-4 mice/group. **b,** Counts

of TCR_{TAG} per organ at 12h, 36h, 48h, and 60h as well as later time points 5 and 21+ days. Each symbol represents an individual mouse with n=3 per group. **** $P<0.0001$ determined by two-way ANOVA with post hoc Šidák multiple comparison test comparing the cumulative number of TCR_{TAG} from tumor-bearing mice and infected mice. **c,** TNF, IFNγ, and CD107a production following 4h *ex vivo* TAG peptide stimulation in TCR_{TAG} from LM_{TAG}-infected mice (green) or from tumor-bearing mice (blue) at pooled 48 and 60h time points. GZMB and PRF1 expression was assessed immediately *ex vivo*. Naive *in vivo* TCR_{TAG} is shown for comparison (N; grey). Dot plots are concatenated from 3 mice/group. **d,** IFNγ and TNF production by TCR_{TAG} from spleens and livers of LM_{TAG}-infected mice at 48h time point following 4h *ex vivo* TAG peptide stimulation (top) and summary plot of percentage $TNF^{+}IFN\gamma^{+}$ TCR_{TAG} (bottom) points where bars represent mean and error bars represent standard deviation. ns = not statistically significant, determined by unpaired two-tailed Student's t-test. **e,** Dot plots of no peptide stimulation controls from infected and tumor-bearing mice from pooled 48 and 60h time points. Two independent experiments were carried out with 2-4 mice/group.

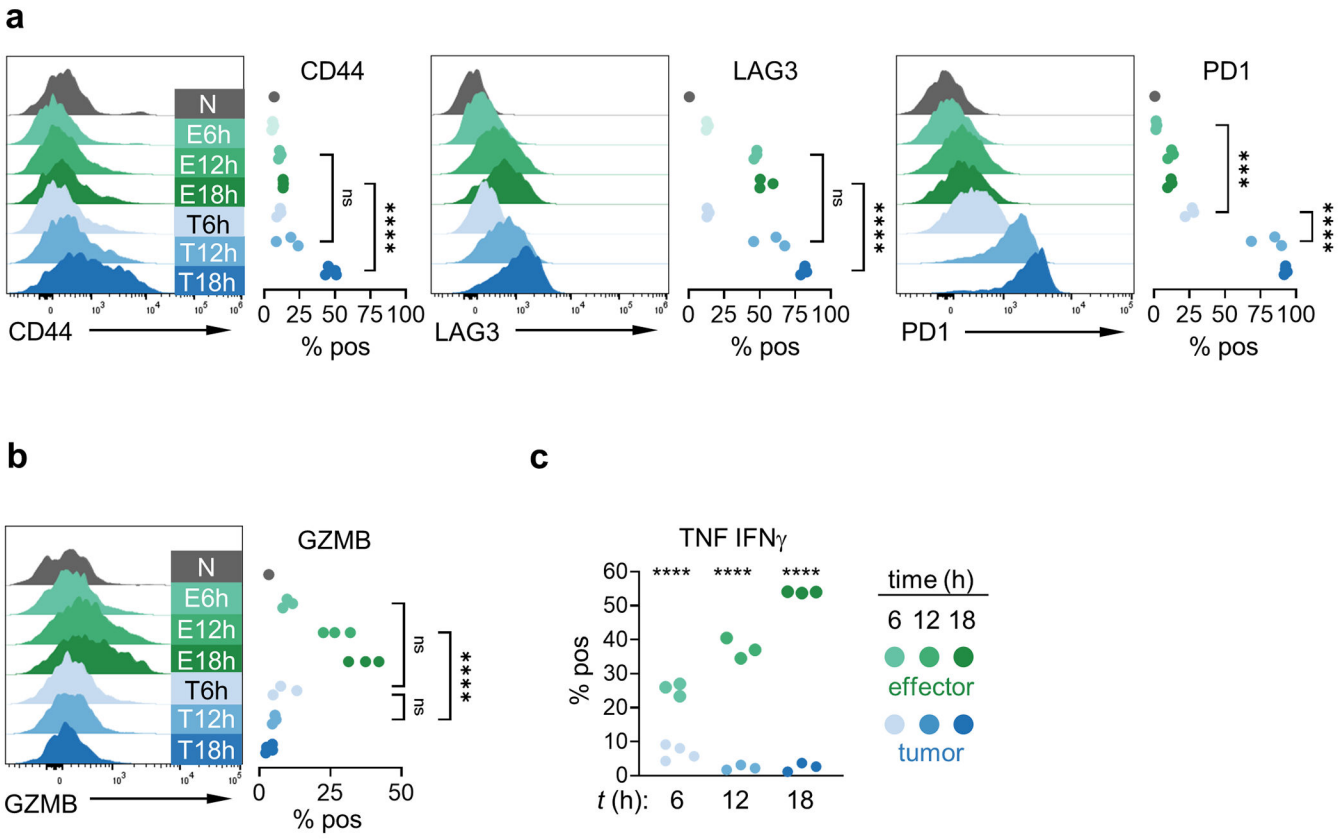

Extended Data Fig. 2: Tumor-induced TST effector function impairment begins prior to cell division.

Live $CD8^{+}$ $Thy1.1^{+}$ TCR_{TAG} analyzed from spleens of infected mice (green) and livers from tumor-bearing hosts (blue) at 6h, 12h, and 18h. **a,** Representative histograms of CD44, LAG3, and PD1 expression profiles. Two independent experiments were carried out with 3-4 mice/group. **b,** *Ex vivo* GZMB expression. Summary plots are shown to the right with each

point representing an individual mouse and n=3-4 per group. **c,** Independent experimental replicate of Fig. 2e showing summary plots of percentage $TNF^{+}IFN\gamma^{+}$ TCR_{TAG} after peptide stimulation. Each symbol represents an individual mouse with n=3-4 per group. ***P=0.0003, ****P <0.0001 determined by two-way ANOVA with post hoc Tukey test.

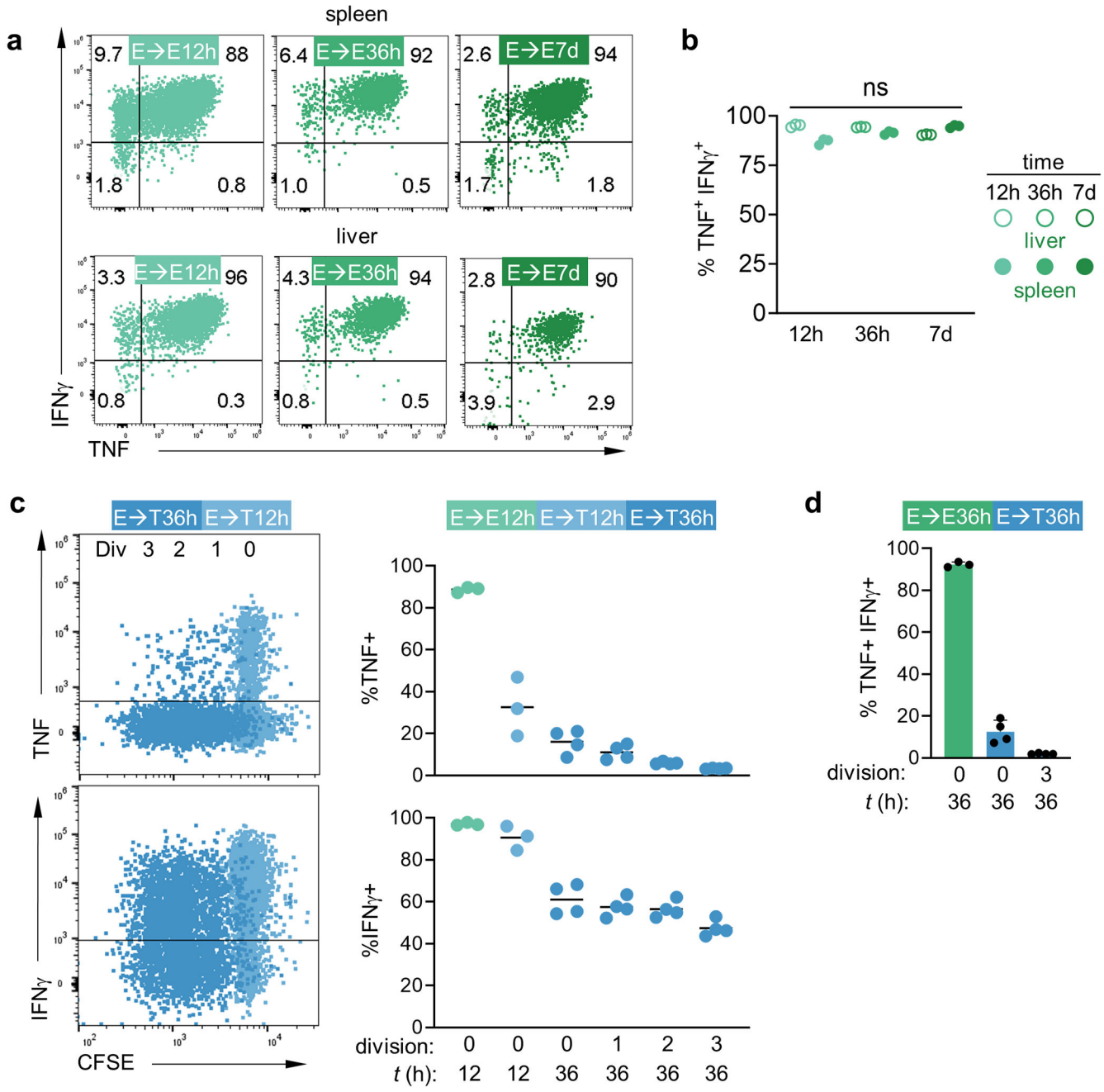

Extended Data Fig. 3: Committed effector CD8 T cells rapidly lose function in tumor-bearing hosts.

Dot plots of TCR_{TAG} TNF and IFNγ production from spleens and livers of LM_{TAG}-infected animals following 4h TAG peptide stimulation. Gates set based on no peptide stimulation

controls. **b,** Summary plots of percentage $TNF^{+}IFN\gamma^{+}$ TCR_{TAG} following 4h TAG peptide stimulation, where open circles represent TCR_{TAG} isolated from livers and closed circles from spleens of infected mice with n=3 (12h, 7d) or 4 (36h) per group. Each point represents an individual animal, statistics determined by two-way ANOVA with post-hoc Tukey test. **c**, TCR_{TAG} CFSE dilution and TNF and IFNγ production at 12h and 36h time points from tumor livers following 4h TAG peptide stimulation (left). Data is concatenated from 3-4 biological replicates/timepoint. Summary plots of percentage $TNF^{+}IFN\gamma^{+}$ TCR_{TAG} (right) where each symbol represents an individual mouse with n=3 (12h) or 4 (36h) per group and black bars represent mean. **d,** Summary plots of percentage $TNF^{+}IFN\gamma^{+}$ TCR_{TAG} by cell division 36h post-transfer points where bars represent mean and error bars represent standard deviation. Each symbol represents an individual mouse with n=3-4 per group.

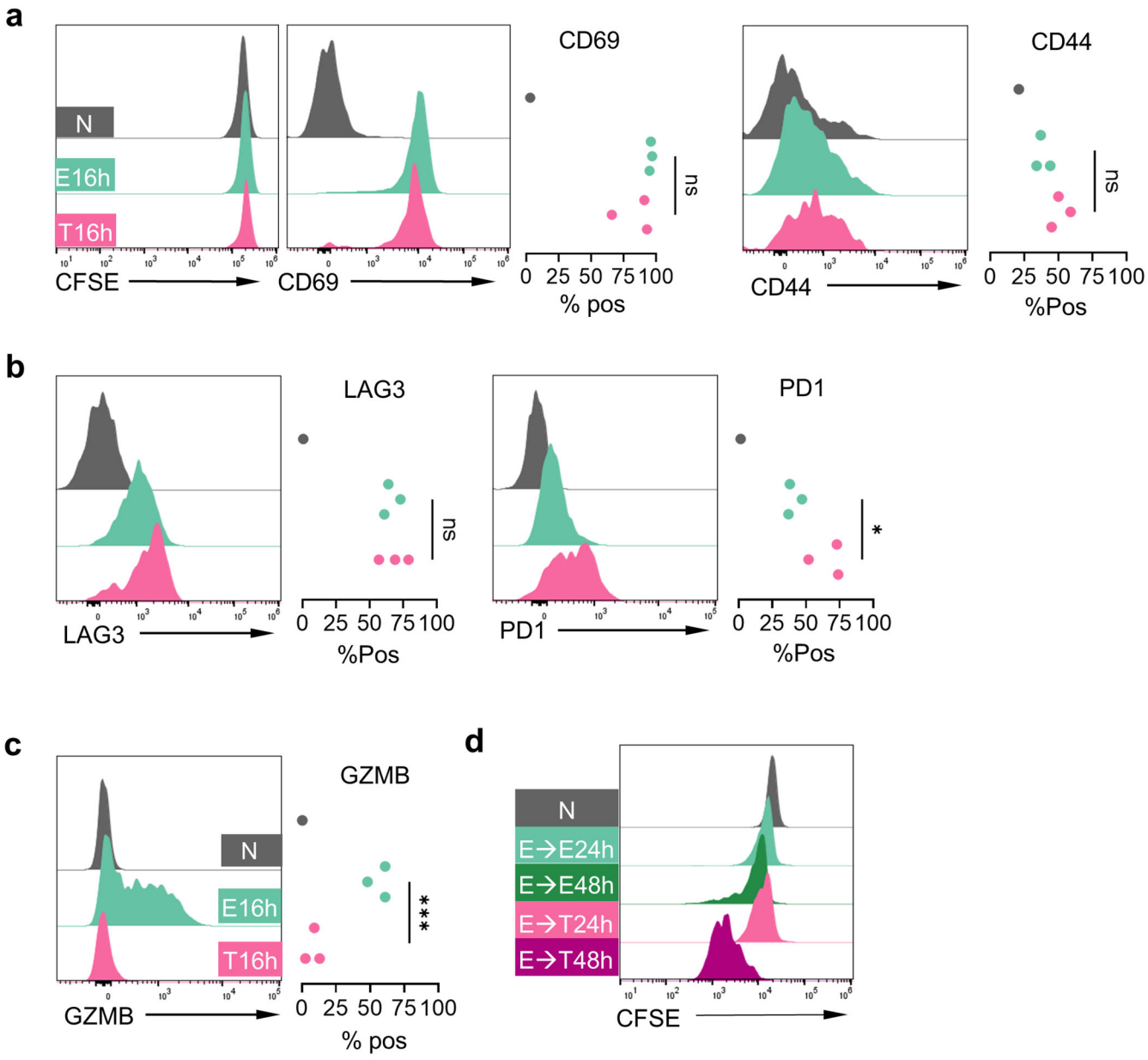

Extended Data Fig. 4: Naive and effector TST robustly proliferate in mice with metastatic melanoma but lack effector function.

Live $CD8^+$ $Ly5.1^+$ TCR_{OTI} analyzed from spleens of LM_{OVA} infected B6 (green) and B6 with pulmonary B16-OVA metastases (pink) at 16h. **a,** Representative histograms of CFSE, CD69, and CD44 expression profiles. **b,** Representative histograms of LAG3 and PD1 expression. **c,** *Ex vivo* GZMB expression. Summary plots are shown to the right with each point representing an individual mouse. **d,** CFSE dilution of E5d TCR_{OTI} transferred into time-matched LM_{OVA} infected B6 (green) or B6 with pulmonary B16-OVA metastases (pink) at 24 and 48 hours following transfer. Naive TCR_{OTI} (N; grey) shown for comparison. *P=0.0307 and ***P=0.0008 determined using unpaired two-tailed Student's t-test.

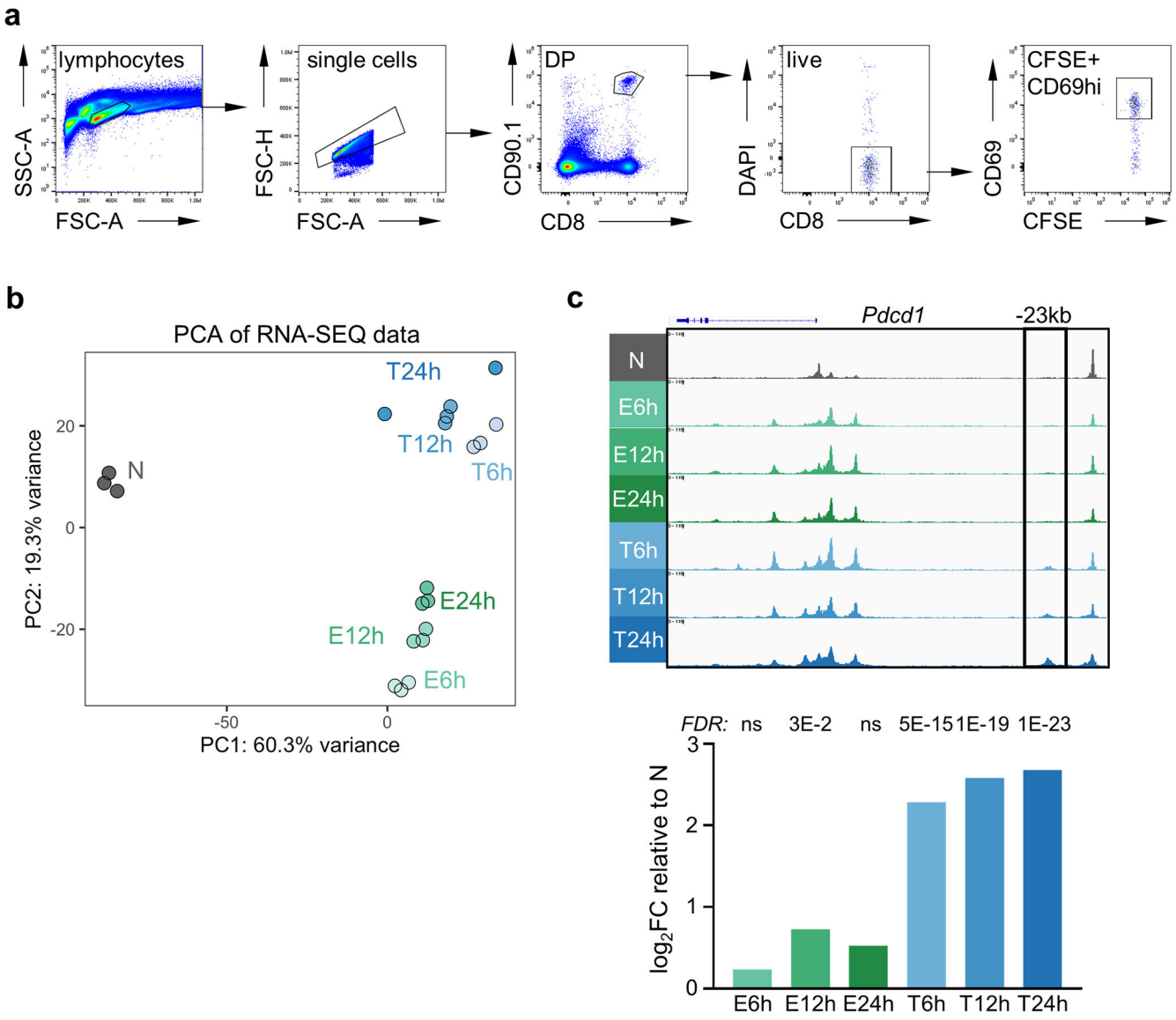

Extended Data Fig. 5. Gating strategy for sorting; dysfunction-associated epigenetic and transcriptional programming begins prior to cell division.

a, Gating strategy to sort TCR_{TAG} from infected spleens or tumor livers for sequencing studies. **b,** Principal component analysis (PCA) of RNA-SEQ data comparing top 500 most variable genes between naive (N; grey) and TCR_{TAG} differentiating during acute infection (green) and in tumors (blue) at 6, 12, 24h post-transfer. Each symbol represents a single biological replicate. **c,** Chromatin accessibility profile across the *Pdcd1* locus with the exhaustion-associated −23kb peak boxed (left). Summary plot (right) shows the DESeq2-determined log_2FC and *FDR* (two-sided Wald test with Benjamini-Hochberg correction) at the *Pdcd1* −23kb peak for early E and T time points as compared to naive (N).

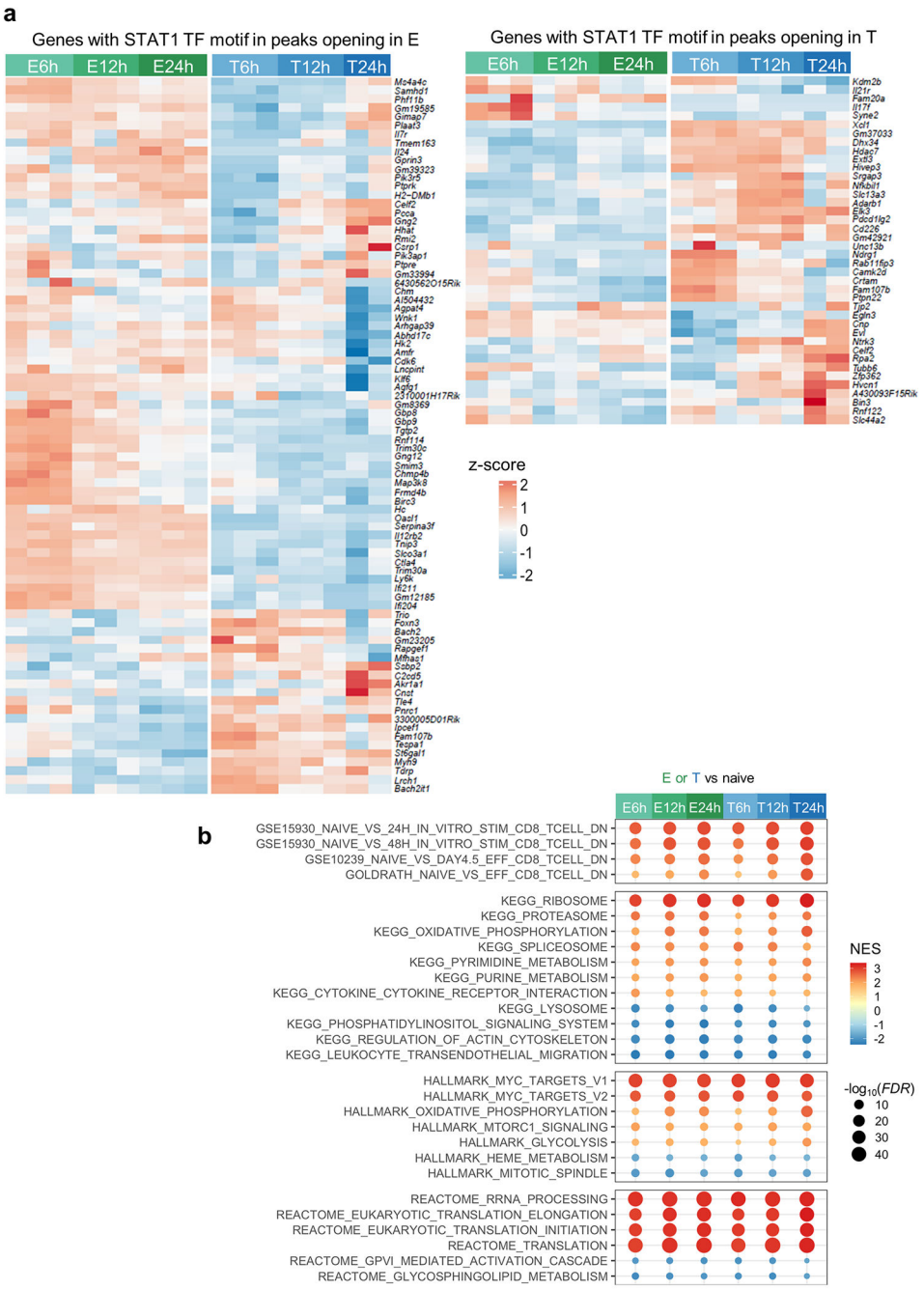

Extended Data Fig. 6: STAT1 motif enrichment is accompanied by increased gene expression in CD8 T cells activated during acute infection; tumor- and infection-activated CD8 T cells show similar enrichment of T cell activation-associated genes.

a, Heatmap showing expression of differentially-expressed genes with peaks containing STAT1 motifs (by ChromVar; Fig. 5e) in effector (E, left) or tumor (T, right) across time points. Heatmaps are z-score normalized across rows. **b,** Gene set enrichment analysis (GSEA) of E versus N or T versus N at 6h, 12h, and 24h post transfer for activation associated gene sets and KEGG, HALLMARK, and REACTOME gene sets.

Color represents normalized enrichment score (NES) and circle size represents the negative $\log_{10}$ (*FDR*).

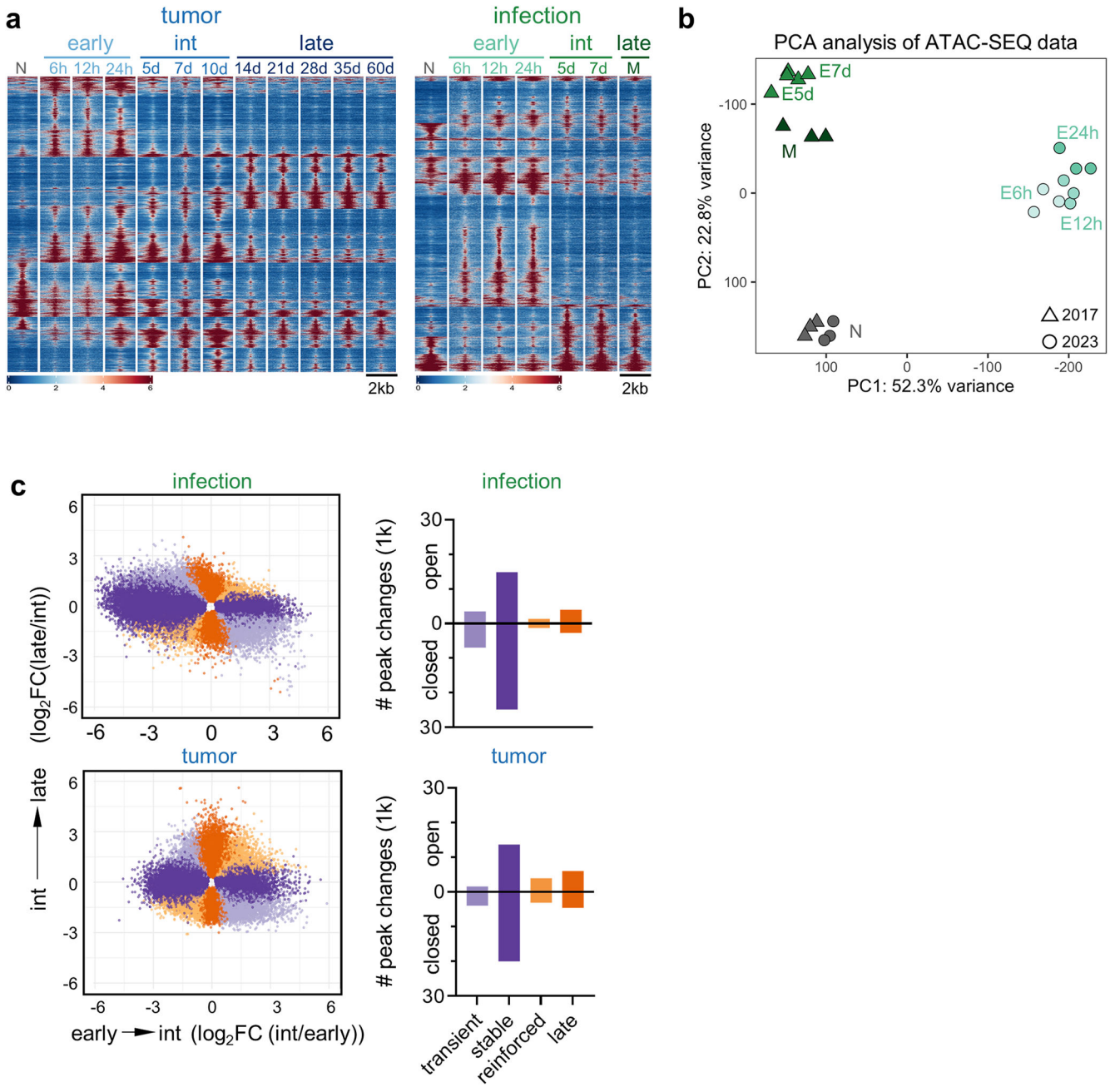

Extended Data Fig. 7: Pre-division tumor-induced TST chromatin remodeling is reinforced with time and tumor antigen exposure.

a, Chromatin accessibility heatmap showing naive (N) and TCR_{TAG} from 6h to 60+d in liver tumors of ASTxCre (left) and in LM_{TAG}-infected B6 (right). Each row represents one of 29,884 (left) or 31,756 (right) peaks (differentially accessible between at least one sequential time point comparison; *FDR* <0.05, $|\log_2 FC| > 1.5$) displayed over 2kb window centered

on the peak summit. Scale units are RPGC normalized to 1x sequencing depth for 20 bp bins with blue indicating closed chromatin and red open chromatin. Peaks are clustered by k-means (k=6). **b,** PCA comparing chromatin accessibility in TCR_{TAG} from 6h to M during infection. Each symbol represents a single biological replicate. **c,** Upper panel shows peak changes for early (E24h) → intermediate (E5d) transition (log_2FC E5d/E24h) versus int (E7d) → late (M) transition (log_2FC M/E7d) (upper). Lower panel shows peak changes for early (T24h) → int (T5d) transition (log_2FC T5d/T24h) versus int (T7d) → late (T14d) transition (log_2FC T14d/T7d). Each point represents an individual peak colored according to the scheme in Fig. 5c. To the right are shown corresponding bar plots showing the number of peaks in e

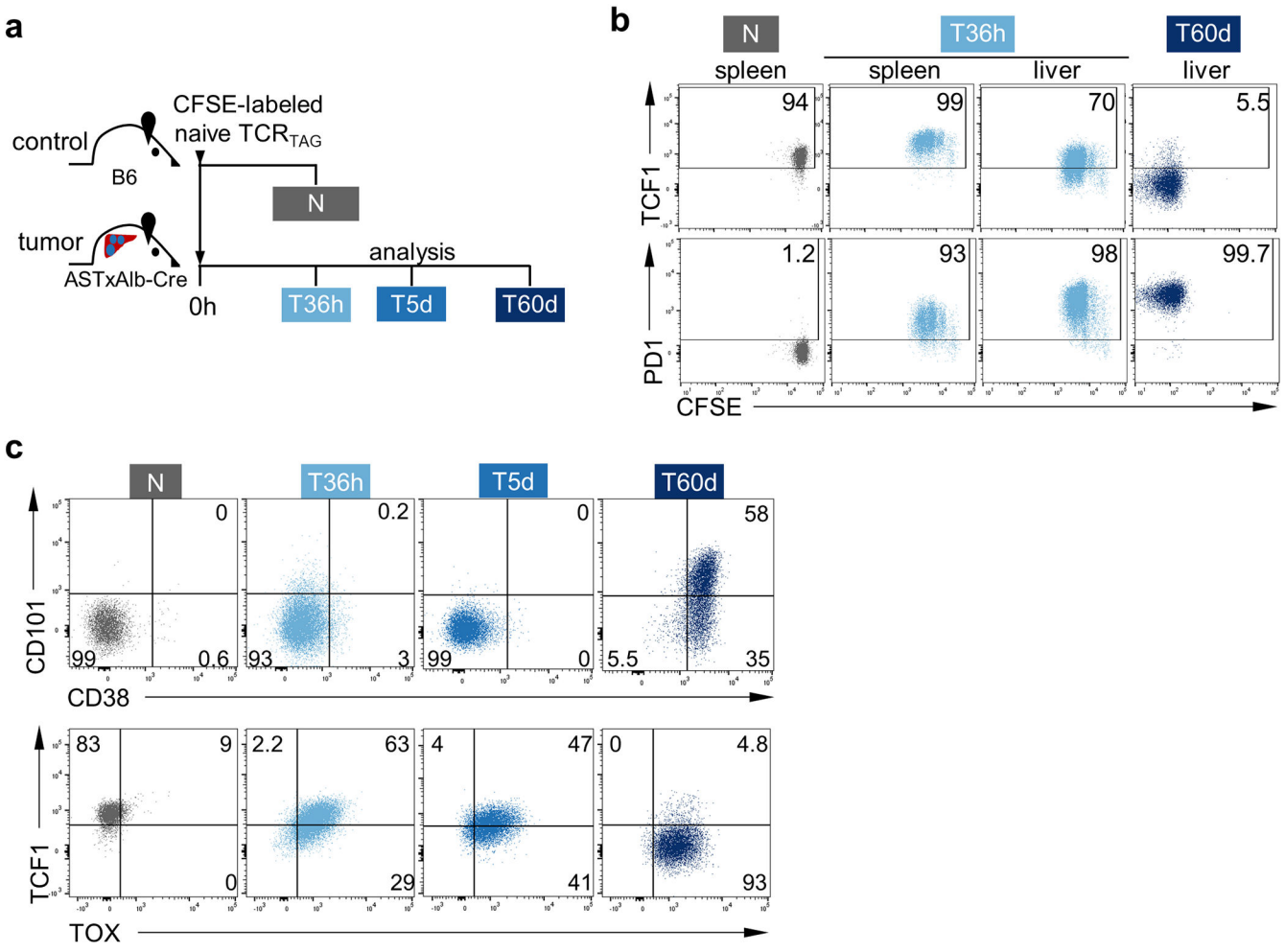

Extended Data Fig. 8: Early TST uniformly express TCF1.

a, Experimental scheme: CFSE-labeled naive TCR_{TAG} (Thy1.1) were adoptively transferred into B6 (Thy1.2) or ASTxAlb-Cre mice (Thy1.2). TCR_{TAG} were re-isolated at 36h (T36h), 5d (T5d), and 60d (T60d) from spleens and livers for flow cytometric analysis (Naive *in vivo* (N; grey); tumor (T; blue)). **b,** Dot plots of TST TCF1 and PD1 expression by CFSE dilution across time points. **c,** Dot plots comparing CD38 and CD101 (top) or TOX and TCF1 (bottom) expression in TST isolated from tumor-bearing livers across time points.

Gates set based on N with inset numbers indicating percentage of cells in each gate. Plots are concatenated from 3-4 samples/time point.

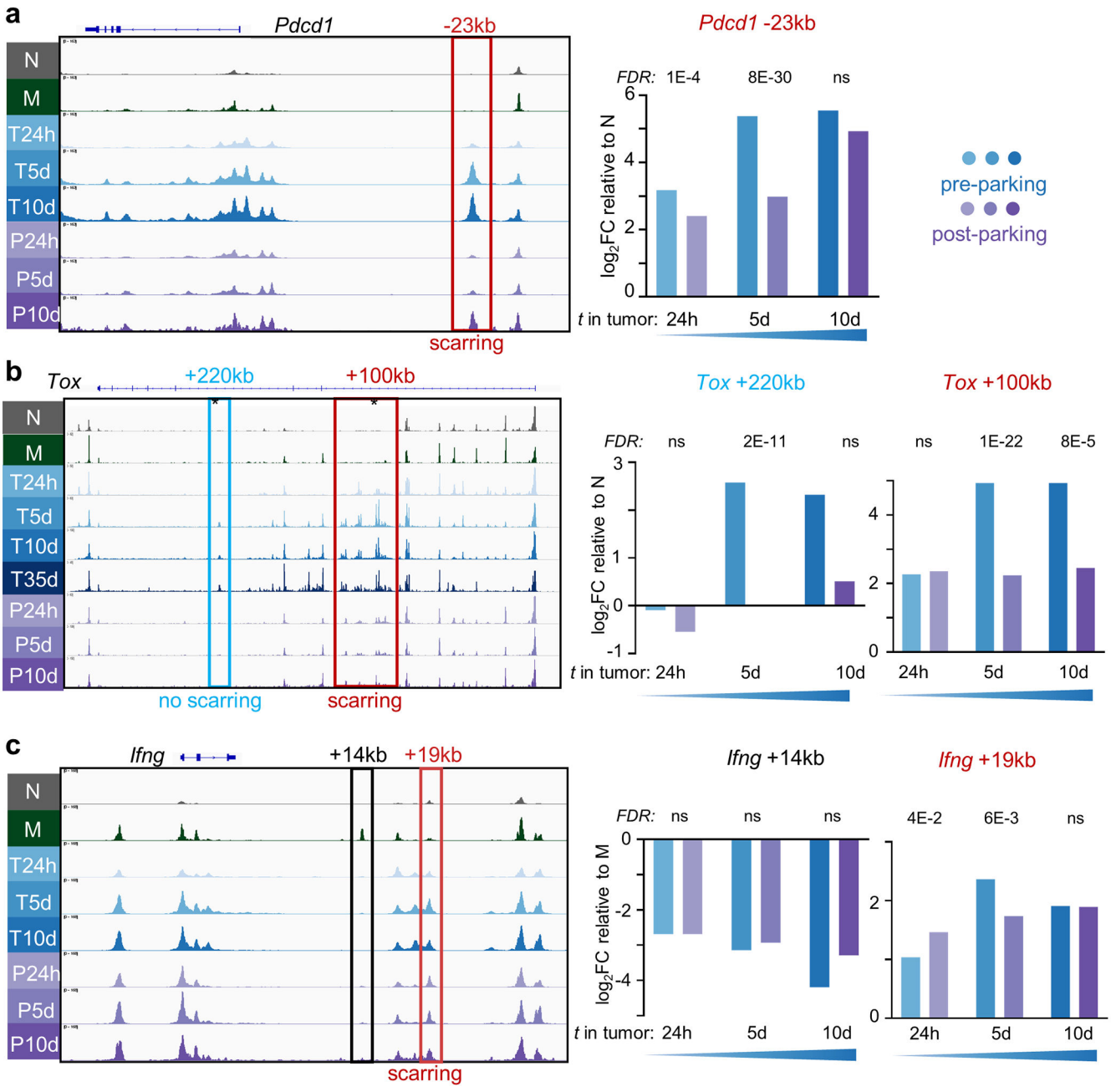

Extended Data Fig. 9: Duration of tumor antigen exposure determines dysfunction stability and imprinting.

Chromatin accessibility profiles across selected gene loci for TCR_{TAG} activated in tumor for 24h (T24h), 5d (T5d), 10d (T10d) pre-parking (blue) and post-parking (P24h, P5d, P10d) (purple) with naive (grey) and memory (green). **a,** *Pdcd1* gene locus with −23 kb enhancer peak boxed in red. Summary plot (right) shows the DESeq2-determined log_2FC and *FDR* (two-sided Wald test with Benjamini-Hochberg correction) at the *Pdcd1* −23kb peak for

pre- (blue) and post-park (purple) relative to naive. **b,** *Tox* locus with blue box representing region without epigenetic scarring and red box showing region with epigenetic scarring. Star denotes representative +100 kb peak from scar region used for quantification on right. Late dysfunctional TCR_{TAG} activated in tumor (D35) added for comparison. Summary plot (right) shows the DESeq2-determined log_2FC and *FDR* (two-sided Wald test with Benjamini-Hochberg correction) at the *Tox* +220 kb and +100 kb peaks for pre- (blue) and post-park (purple) relative to naive. **c,** *Ifng* locus with black box denoting +14kb peak open in memory but not in pre- or post-parking samples, and red box denoting +19kb peak open in both pre- and post-parking samples. Summary plot (right) shows the DESeq2-determined log_2FC and *FDR* (two-sided Wald test with Benjamini-Hochberg correction) for the *Ifng* +14kb and +19 kb peak area pre- (blue) and post-park (purple) relative to memory.

Supplementary Material

Refer to Web version on PubMed Central for supplementary material.

ACKNOWLEDGEMENTS

We thank A. Schietinger and members of the Philip laboratory for helpful discussions. We thank E. Chiu, A. Dave, G. Anzarova, and T. Bryson for technical assistance. We thank the Vanderbilt Division of Animal Care, D. Flaherty and the Vanderbilt University Medical Center Flow (VUMC) Cytometry Shared Resource Core, A. Jones and the Vanderbilt Technologies for Advanced Genomics (VANTAGE) Core, and A. Viale and the Sloan Kettering Integrated Genomics Operation Core (IGO). We thank P. Lauer and Aduro Biotech for providing attenuated *Listeria* strains. We thank A. Schietinger, J.C. Rathmell and J.M. Balko for critical review of the manuscript. This work was supported by the following funding sources: V Foundation Scholar Award (M.P.), NIH R37CA263614 (M.P.), Serodino Family Adventure Allee Fund (M.P.), Vanderbilt-Ingram Cancer Center (VICC) SPORE Career Enhancement Program (M.P.) NIH P50CA098131, Vanderbilt Digestive Disease Research Center (VDDRC) Young Investigator and Pilot Award (M.P.) NIH P30DK058404, Medical Scientist Training Program (MSTP) NIH T32GM007347 (M.W.R.), NIH T32GM008554 (N.R.F.), NIH T32CA009592 (C.R.D.R), and NIH T32AR059039 (M.M.E.). The VUMC Flow Cytometry Shared Resource is supported by the VICC (NIH P30CA68485) and the VDDRC (NIH P30DK058404). VANTAGE is supported by the VICC (NIH P30CA68485), the Vanderbilt Vision Center (NIH P30EY08126) and the NIH G20RR030956. IGO is supported by NIH P30CA08748, Cycle for Survival, and the Marie-Josée and Henry R. Kravis Center for Molecular Oncology.

DATA AVAILABILITY

The RNA-SEQ and ATAC-SEQ data have been deposited in the Gene Expression Omnibus (GEO Super-Series accession number GSE209712). KEGG, HALLMARK, and REACTOME gene sets were retrieved from the Broad Institute's MSigDB collections using msigbr v7.5.177(https://www.gsea-msigdb.org/gsea/msigdb/index.jsp). Source data are provided with the paper. All other data that support the findings of this study are present in the article or are available from the corresponding author (MP) upon request.

REFERENCES

1. Williams MA & Bevan MJ Effector and memory CTL differentiation. Annu Rev Immunol 25, 171–192 (2007). [PubMed: 17129182]
2. McLane LM, Abdel-Hakeem MS & Wherry EJ CD8 T Cell Exhaustion During Chronic Viral Infection and Cancer. Annu Rev Immunol (2019).
3. Waugh KA et al. Molecular Profile of Tumor-Specific CD8+ T Cell Hypofunction in a Transplantable Murine Cancer Model. Journal of immunology 197, 1477–1488 (2016).
4. Mognol GP et al. Exhaustion-associated regulatory regions in CD8+ tumor-infiltrating T cells. Proc Natl Acad Sci U S A 114, E2776–E2785 (2017). [PubMed: 28283662]

5. Philip M et al. Chromatin states define tumour-specific T cell dysfunction and reprogramming. Nature 545, 452–456 (2017). [PubMed: 28514453]
6. Zhu L & Skoultchi AI Coordinating cell proliferation and differentiation. Curr Opin Genet Dev 11, 91–97 (2001). [PubMed: 11163157]
7. Kreslavsky T et al. beta-Selection-Induced Proliferation Is Required for alphabeta T Cell Differentiation. Immunity 37, 840–853 (2012). [PubMed: 23159226]
8. Bird JJ et al. Helper T cell differentiation is controlled by the cell cycle. Immunity 9, 229–237 (1998). [PubMed: 9729043]
9. Tangye SG & Hodgkin PD Divide and conquer: the importance of cell division in regulating B-cell responses. Immunology 112, 509–520 (2004). [PubMed: 15270721]
10. Scharer CD, Barwick BG, Guo M, Bally APR & Boss JM Plasma cell differentiation is controlled by multiple cell division-coupled epigenetic programs. Nature communications 9, 1698 (2018).
11. Kaech SM & Ahmed R Memory CD8+ T cell differentiation: initial antigen encounter triggers a developmental program in naive cells. Nat Immunol 2, 415–422 (2001). [PubMed: 11323695]
12. van Stipdonk MJ, Lemmens EE & Schoenberger SP Naive CTLs require a single brief period of antigenic stimulation for clonal expansion and differentiation. Nat Immunol 2, 423–429 (2001). [PubMed: 11323696]
13. Williams MA & Bevan MJ Shortening the infectious period does not alter expansion of CD8 T cells but diminishes their capacity to differentiate into memory cells. Journal of immunology 173, 6694–6702 (2004).
14. Bevan MJ & Fink PJ The CD8 response on autopilot. Nat Immunol 2, 381–382 (2001). [PubMed: 11323687]
15. Schietinger A et al. Tumor-Specific T Cell Dysfunction Is a Dynamic Antigen-Driven Differentiation Program Initiated Early during Tumorigenesis. Immunity 45, 389–401 (2016). [PubMed: 27521269]
16. Philip M & Schietinger A CD8(+) T cell differentiation and dysfunction in cancer. Nat Rev Immunol 22, 209–223 (2022). [PubMed: 34253904]
17. Scott AC et al. TOX is a critical regulator of tumour-specific T cell differentiation. Nature 571, 270–274 (2019). [PubMed: 31207604]
18. Okazaki T et al. PD-1 and LAG-3 inhibitory co-receptors act synergistically to prevent autoimmunity in mice. J Exp Med 208, 395–407 (2011). [PubMed: 21300912]
19. Ahn E et al. Role of PD-1 during effector CD8 T cell differentiation. Proc Natl Acad Sci U S A 115, 4749–4754 (2018). [PubMed: 29654146]
20. Wherry EJ, Blattman JN, Murali-Krishna K, van der Most R & Ahmed R Viral persistence alters CD8 T-cell immunodominance and tissue distribution and results in distinct stages of functional impairment. J Virol 77, 4911–4927 (2003). [PubMed: 12663797]
21. Buenrostro JD, Giresi PG, Zaba LC, Chang HY & Greenleaf WJ Transposition of native chromatin for fast and sensitive epigenomic profiling of open chromatin, DNA-binding proteins and nucleosome position. Nature methods 10, 1213–1218 (2013). [PubMed: 24097267]
22. Sen DR et al. The epigenetic landscape of T cell exhaustion. Science 354, 1165–1169 (2016). [PubMed: 27789799]
23. Pauken KE et al. Epigenetic stability of exhausted T cells limits durability of reinvigoration by PD-1 blockade. Science 354, 1160–1165 (2016). [PubMed: 27789795]
24. Scott-Browne JP et al. Dynamic Changes in Chromatin Accessibility Occur in CD8+ T Cells Responding to Viral Infection. Immunity 45, 1327–1340 (2016). [PubMed: 27939672]
25. Schep AN, Wu B, Buenrostro JD & Greenleaf WJ chromVAR: inferring transcription-factor-associated accessibility from single-cell epigenomic data. Nature methods 14, 975–978 (2017). [PubMed: 28825706]
26. Deng W et al. Recombinant Listeria promotes tumor rejection by CD8(+) T cell-dependent remodeling of the tumor microenvironment. Proc Natl Acad Sci U S A 115, 8179–8184 (2018). [PubMed: 30038013]
27. Harty JT, Tvinnereim AR & White DW CD8+ T cell effector mechanisms in resistance to infection. Annu Rev Immunol 18, 275–308 (2000). [PubMed: 10837060]

28. Sadler AJ & Williams BR Interferon-inducible antiviral effectors. Nat Rev Immunol 8, 559–568 (2008). [PubMed: 18575461]
29. Martinez GJ et al. The transcription factor NFAT promotes exhaustion of activated CD8(+) T cells. Immunity 42, 265–278 (2015). [PubMed: 25680272]
30. Chapman NM, Boothby MR & Chi H Metabolic coordination of T cell quiescence and activation. Nat Rev Immunol 20, 55–70 (2020). [PubMed: 31406325]
31. Tsao HW et al. Batf-mediated epigenetic control of effector CD8(+) T cell differentiation. Sci Immunol 7, eabi4919 (2022). [PubMed: 35179948]
32. Yang CY et al. The transcriptional regulators Id2 and Id3 control the formation of distinct memory CD8+ T cell subsets. Nat Immunol 12, 1221–1229 (2011). [PubMed: 22057289]
33. Roychoudhuri R et al. BACH2 regulates CD8(+) T cell differentiation by controlling access of AP-1 factors to enhancers. Nat Immunol 17, 851–860 (2016). [PubMed: 27158840]
34. Machlab D et al. monaLisa: an R/Bioconductor package for identifying regulatory motifs. Bioinformatics 38, 2624–2625 (2022). [PubMed: 35199152]
35. Intlekofer AM et al. Anomalous type 17 response to viral infection by CD8+ T cells lacking T-bet and eomesodermin. Science 321, 408–411 (2008). [PubMed: 18635804]
36. Intlekofer AM et al. Effector and memory CD8+ T cell fate coupled by T-bet and eomesodermin. Nat Immunol 6, 1236–1244 (2005). [PubMed: 16273099]
37. Sullivan BM, Juedes A, Szabo SJ, von Herrath M & Glimcher LH Antigen-driven effector CD8 T cell function regulated by T-bet. Proc Natl Acad Sci U S A 100, 15818–15823 (2003). [PubMed: 14673093]
38. Pearce EL et al. Control of effector CD8+ T cell function by the transcription factor Eomesodermin. Science 302, 1041–1043 (2003). [PubMed: 14605368]
39. He R et al. Follicular CXCR5- expressing CD8(+) T cells curtail chronic viral infection. Nature 537, 412–428 (2016). [PubMed: 27501245]
40. Im SJ et al. Defining CD8+ T cells that provide the proliferative burst after PD-1 therapy. Nature 537, 417–421 (2016). [PubMed: 27501248]
41. Utzschneider DT et al. T Cell Factor 1-Expressing Memory-like CD8(+) T Cells Sustain the Immune Response to Chronic Viral Infections. Immunity 45, 415–427 (2016). [PubMed: 27533016]
42. Wu T et al. The TCF1-Bcl6 axis counteracts type I interferon to repress exhaustion and maintain T cell stemness. Sci Immunol 1 (2016).
43. Philip M & Schietinger A CD8(+) T cell differentiation and dysfunction in cancer. Nat Rev Immunol (2021).
44. Abdel-Hakeem MS et al. Epigenetic scarring of exhausted T cells hinders memory differentiation upon eliminating chronic antigenic stimulation. Nat Immunol 22, 1008–1019 (2021). [PubMed: 34312545]
45. Hensel N et al. Memory-like HCV-specific CD8(+) T cells retain a molecular scar after cure of chronic HCV infection. Nat Immunol 22, 229–239 (2021). [PubMed: 33398179]
46. Yates KB et al. Epigenetic scars of CD8(+) T cell exhaustion persist after cure of chronic infection in humans. Nat Immunol 22, 1020–1029 (2021). [PubMed: 34312547]
47. Liu J et al. CTCF mediates CD8+ effector differentiation through dynamic redistribution and genomic reorganization. J Exp Med 220 (2023).
48. Amezquita RA marge: An API for Analysis of Motifs Using HOMER in R. 2019.
49. Cao Z, Sun X, Icli B, Wara AK & Feinberg MW Role of Kruppel-like factors in leukocyte development, function, and disease. Blood 116, 4404–4414 (2010). [PubMed: 20616217]
50. Yamada T, Park CS, Mamonkin M & Lacorazza HD Transcription factor ELF4 controls the proliferation and homing of CD8+ T cells via the Kruppel-like factors KLF4 and KLF2. Nat Immunol 10, 618–626 (2009). [PubMed: 19412182]
51. Guan T et al. ZEB1, ZEB2, and the miR-200 family form a counterregulatory network to regulate CD8(+) T cell fates. J Exp Med 215, 1153–1168 (2018). [PubMed: 29449309]

52. Omilusik KD et al. Transcriptional repressor ZEB2 promotes terminal differentiation of CD8+ effector and memory T cell populations during infection. J Exp Med 212, 2027–2039 (2015). [PubMed: 26503445]
53. Scott CL & Omilusik KD ZEBs: Novel Players in Immune Cell Development and Function. Trends Immunol 40, 431–446 (2019). [PubMed: 30956067]
54. Shih HY et al. Developmental Acquisition of Regulomes Underlies Innate Lymphoid Cell Functionality. Cell 165, 1120–1133 (2016). [PubMed: 27156451]
55. Hernandez J, Aung S, Marquardt K & Sherman LA Uncoupling of proliferative potential and gain of effector function by CD8(+) T cells responding to self-antigens. J Exp Med 196, 323–333 (2002). [PubMed: 12163561]
56. Curtsinger JM, Lins DC & Mescher MF Signal 3 determines tolerance versus full activation of naive CD8 T cells: dissociating proliferation and development of effector function. J Exp Med 197, 1141–1151 (2003). [PubMed: 12732656]
57. Otten GR & Germain RN Split anergy in a CD8+ T cell: receptor-dependent cytolysis in the absence of interleukin-2 production. Science 251, 1228–1231 (1991). [PubMed: 1900952]
58. Belk JA et al. Genome-wide CRISPR screens of T cell exhaustion identify chromatin remodeling factors that limit T cell persistence. Cancer Cell 40, 768–786 e767 (2022). [PubMed: 35750052]
59. Guo A et al. cBAF complex components and MYC cooperate early in CD8(+) T cell fate. Nature 607, 135–141 (2022). [PubMed: 35732731]
60. Legut M et al. A genome-scale screen for synthetic drivers of T cell proliferation. Nature 603, 728–735 (2022). [PubMed: 35296855]
61. Utzschneider DT et al. Early precursor T cells establish and propagate T cell exhaustion in chronic infection. Nat Immunol (2020).
62. Wherry EJ et al. Molecular signature of CD8+ T cell exhaustion during chronic viral infection. Immunity 27, 670–684 (2007). [PubMed: 17950003]

METHODS-ONLY REFERENCES

63. Staveley-O'Carroll K et al. In vivo ligation of CD40 enhances priming against the endogenous tumor antigen and promotes CD8+ T cell effector function in SV40 T antigen transgenic mice. Journal of immunology 171, 697–707 (2003).
64. Stahl S et al. Tumor agonist peptides break tolerance and elicit effective CTL responses in an inducible mouse model of hepatocellular carcinoma. Immunol Lett 123, 31–37 (2009). [PubMed: 19428549]
65. Brockstedt DG et al. Listeria-based cancer vaccines that segregate immunogenicity from toxicity. Proc Natl Acad Sci U S A 101, 13832–13837 (2004). [PubMed: 15365184]
66. Andrews S FastQC: a quality control tool for high throughput sequence data. (2010).
67. Hartley SW & Mullikin JC QoRTs: a comprehensive toolset for quality control and data processing of RNA-Seq experiments. BMC Bioinformatics 16, 224 (2015). [PubMed: 26187896]
68. R Core Team. R: A Language and Environment for Statistical Computing R Foundation for Statistical Computing (2017).
69. Wickham H et al. ggplot2: Elegant Graphics for Data Analysis. (2016).
70. Martin M Cutadapt removes adapter sequences from high-throughput sequencing reads. EMBnet.journal 17, 10–12 (2011).
71. Dobin A et al. STAR: ultrafast universal RNA-seq aligner. Bioinformatics 29, 15–21 (2013). [PubMed: 23104886]
72. Liao Y, Smyth GK & Shi W featureCounts: an efficient general purpose program for assigning sequence reads to genomic features. Bioinformatics 30, 923–930 (2014). [PubMed: 24227677]
73. Love MI, Huber W & Anders S Moderated estimation of fold change and dispersion for RNA-seq data with DESeq2. Genome biology 15, 550 (2014). [PubMed: 25516281]
74. Korotkevich G et al. Fast gene set enrichment analysis. bioRxiv, 060012 (2021).

75. Subramanian A et al. Gene set enrichment analysis: a knowledge-based approach for interpreting genome-wide expression profiles. Proc Natl Acad Sci U S A 102, 15545–15550 (2005). [PubMed: 16199517]
76. Liberzon A et al. Molecular signatures database (MSigDB) 3.0. Bioinformatics 27, 1739–1740 (2011). [PubMed: 21546393]
77. Dolgalev I msigdbr: MSigDB Gene Sets for Multiple Organisms in a Tidy Data Format. 2022.
78. Li H & Durbin R Fast and accurate short read alignment with Burrows-Wheeler transform. Bioinformatics 25, 1754–1760 (2009). [PubMed: 19451168]
79. Li H et al. The Sequence Alignment/Map format and SAMtools. Bioinformatics 25, 2078–2079 (2009). [PubMed: 19505943]
80. Liu T Use model-based Analysis of ChIP-Seq (MACS) to analyze short reads generated by sequencing protein-DNA interactions in embryonic stem cells. Methods in molecular biology 1150, 81–95 (2014). [PubMed: 24743991]
81. Stark R & Brown G DiffBind: differential binding analysis of ChIP-Seq peak data. (2011).
82. Yu G, Wang LG & He QY ChIPseeker: an R/Bioconductor package for ChIP peak annotation, comparison and visualization. Bioinformatics 31, 2382–2383 (2015). [PubMed: 25765347]
83. Leek JT et al. sva: Surrogate Variable Analysis. R package version 3.44.0 (2022).
84. Weirauch MT et al. Determination and inference of eukaryotic transcription factor sequence specificity. Cell 158, 1431–1443 (2014). [PubMed: 25215497]
85. Ramirez F et al. deepTools2: a next generation web server for deep-sequencing data analysis. Nucleic Acids Res 44, W160–165 (2016). [PubMed: 27079975]
86. Carroll T & Barrows D profileplyr: Visualization and annotation of read signal over genomic ranges with profileplyr. R package version 1.12.0. (2022).
87. Gu Z, Eils R & Schlesner M Complex heatmaps reveal patterns and correlations in multidimensional genomic data. Bioinformatics 32, 2847–2849 (2016). [PubMed: 27207943]

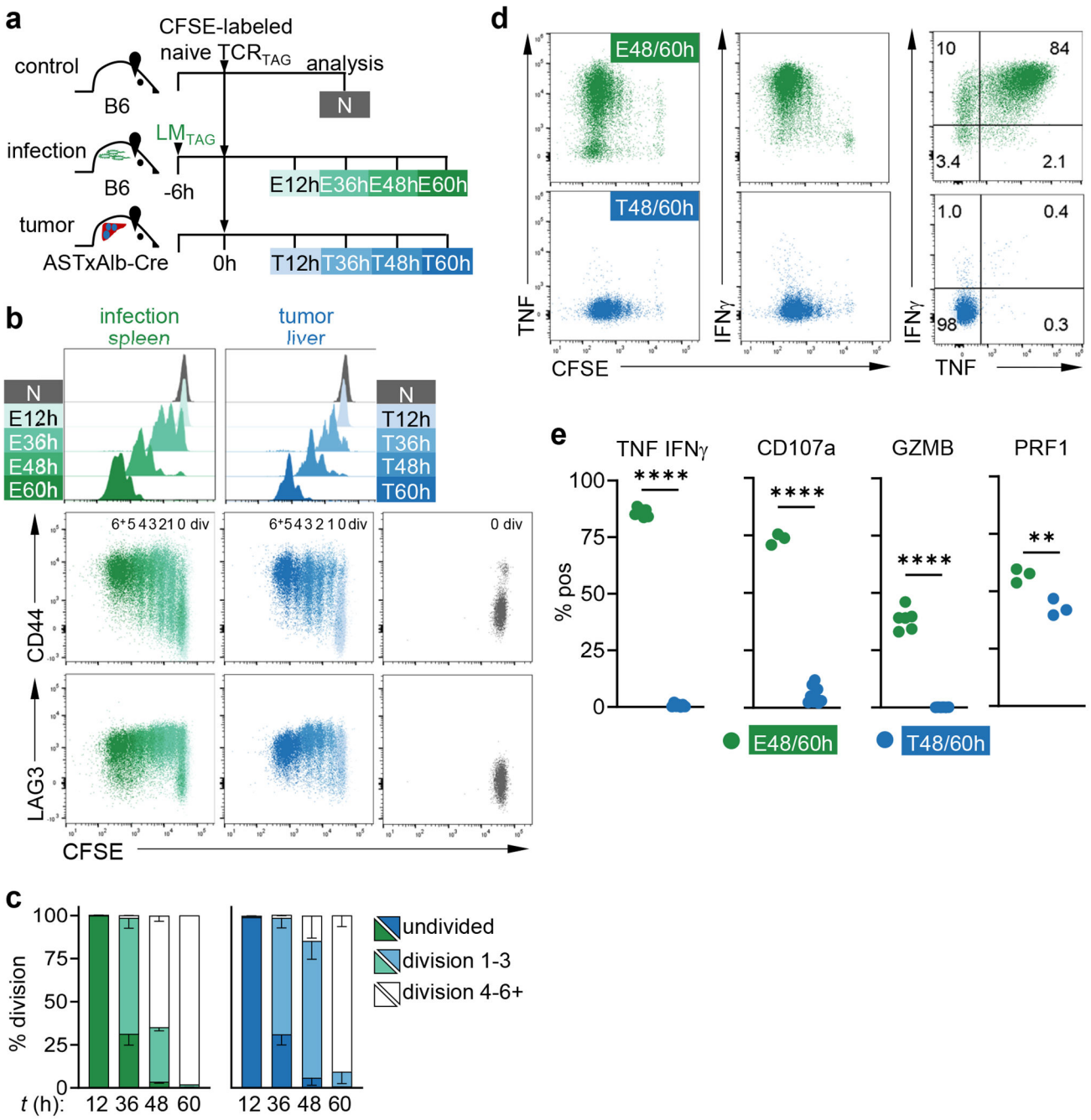

Figure 1|. TST undergo robust activation and proliferation but do not gain effector function.

a, Experimental scheme: CFSE-labeled naive TCR_{TAG} (Thy1.1) were adoptively transferred into B6 (Thy1.2), LM_{TAG}-infected B6 (Thy1.2), or ASTxAlb-Cre (Thy1.2) bearing late-stage liver tumors. TCR_{TAG} were re-isolated at 12, 36, 48, and 60 hours (h) from infected spleen or tumor livers for flow cytometric analysis (Naive *in vivo* (N; grey); Effector (E; green); Tumor (T; blue)). **b**, TCR_{TAG} CFSE dilution assessed at each time point (upper) with CD44 and LAG3 versus CFSE dilution at all time points (lower) shown in comparison to N. All flow plots are gated on live $CD8^+$ $Thy1.1^+$ TCR_{TAG}, and data for each time

point is concatenated from 3-4 biologic replicates. **c**, Summary plot showing percentage of cells that were undivided, completed 1-3, or 3-6+ cell divisions in infected mice (spleens; green) or tumor-bearing mice (livers; blue) at indicated time points with n=3 mice per group. Error bars represent standard deviation. Three independent experiments were performed. **d**, TCR_{TAG} IFNγ and TNF production after 4h *ex vivo* TAG peptide stimulation, assessed by flow cytometry. Inset numbers represent percent of population in each gate. Gates were set based on no peptide stimulation controls; see Extended Data Fig. 1e for representative figure). **e**, Percentage of $TNF^+IFN\gamma^+$ and $CD107a^+$ $CD8^+$ $Thy1.1^+$ TCR_{TAG} (E48/60h and T48/60h) following *ex vivo* TAG peptide stimulation, and granzyme B (GZMB) and perforin (PRF1) expression immediately *ex vivo.* Each symbol represents an individual mouse, n=3-9 pooled from two independent experiments. $^{**}P=0.0066$, $^{****}P<0.0001$ determined using unpaired two-tailed Student's t-test.

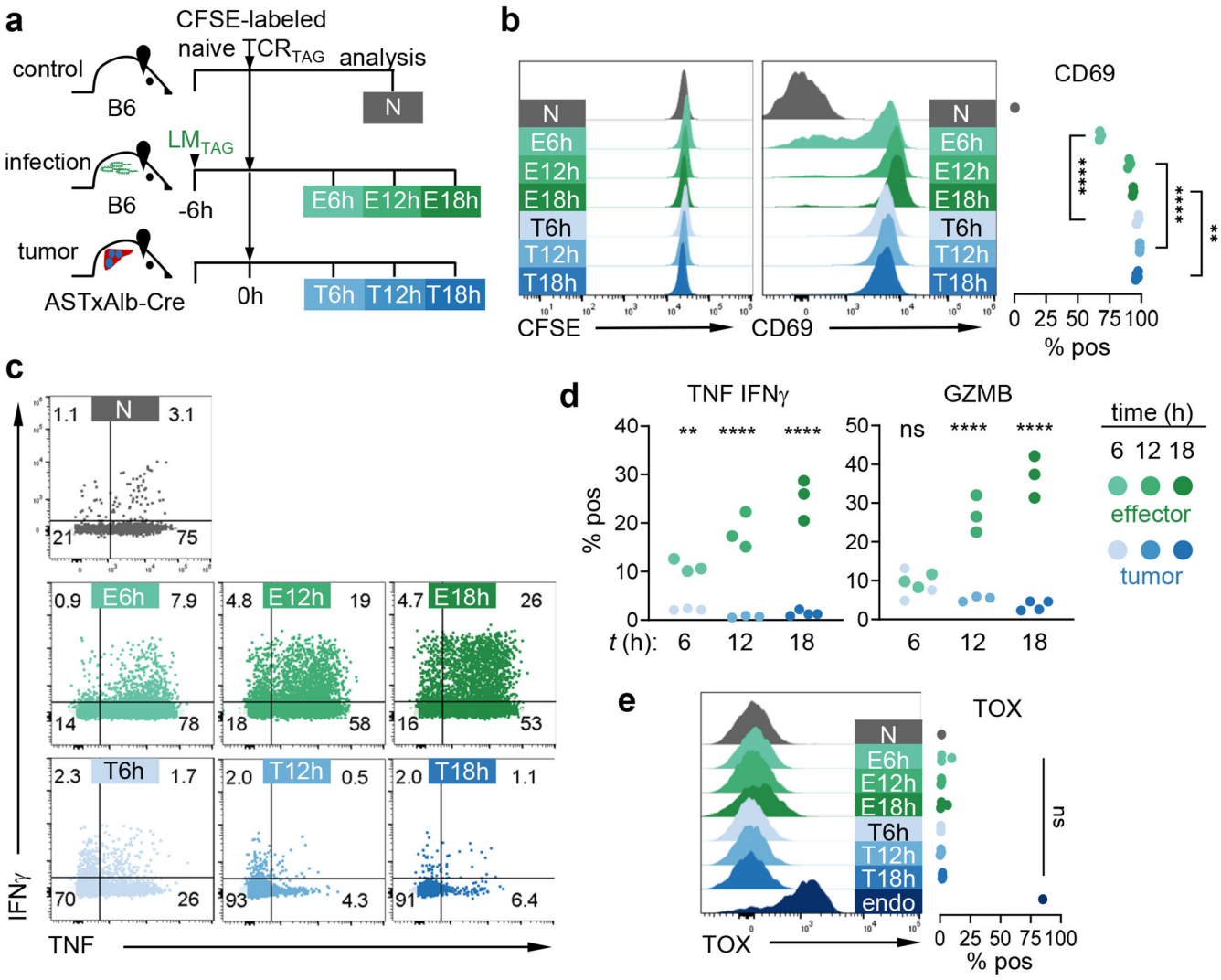

Figure 2|. Tumor-induced TST effector function impairment begins prior to cell division.

a, Experimental scheme: CFSE-labeled naive TCR_{TAG} (Thy1.1) were adoptively transferred into B6 (Thy1.2), LM_{TAG}-infected B6 (Thy1.2), or ASTxAlb-Cre (Thy1.2), and lymphocytes were re-isolated from tumor livers (blue) and infected spleens (green) at 6h, 12h, and 18h post-transfer for analysis by flow cytometry. **b**, Representative histograms of live $CD8^+$ $Thy1.1^+$ TCR_{TAG} CFSE dilution at each time point (left) and histograms and summary plot of CD69 expression (right) shown in comparison to naive *in vivo* (N; grey). $^{**}P$=0.0024, $^{****}P$ <0.0001 determined by two-way ANOVA with post hoc Tukey test. **c**, Representative dot plots of TCR_{TAG} IFNγ and TNF production after 4h *ex vivo* TAG peptide stimulation, with inset numbers indicating percentage of cells in each gate. Gates set based on no peptide stimulation controls. **d**, Summary plots of percentage $TNF^+IFN\gamma^+$ TCR_{TAG} after peptide stimulation and *ex* vivo GZMB expression. Each symbol represents an individual mouse. **e**, Histograms and summary plots of TOX expression. $CD8^+$ $Thy1.1^-$ $PD1^{hi}$ endogenous (endo) dysfunctional T cells are shown as the positive control for TOX staining. Histograms show representative data for each group. ns=not statistically significant,

** P=0.0036, **** P <0.0001 determined by two-way ANOVA with post hoc Tukey test. Two independent experiments were carried out with 3-4 mice/group.

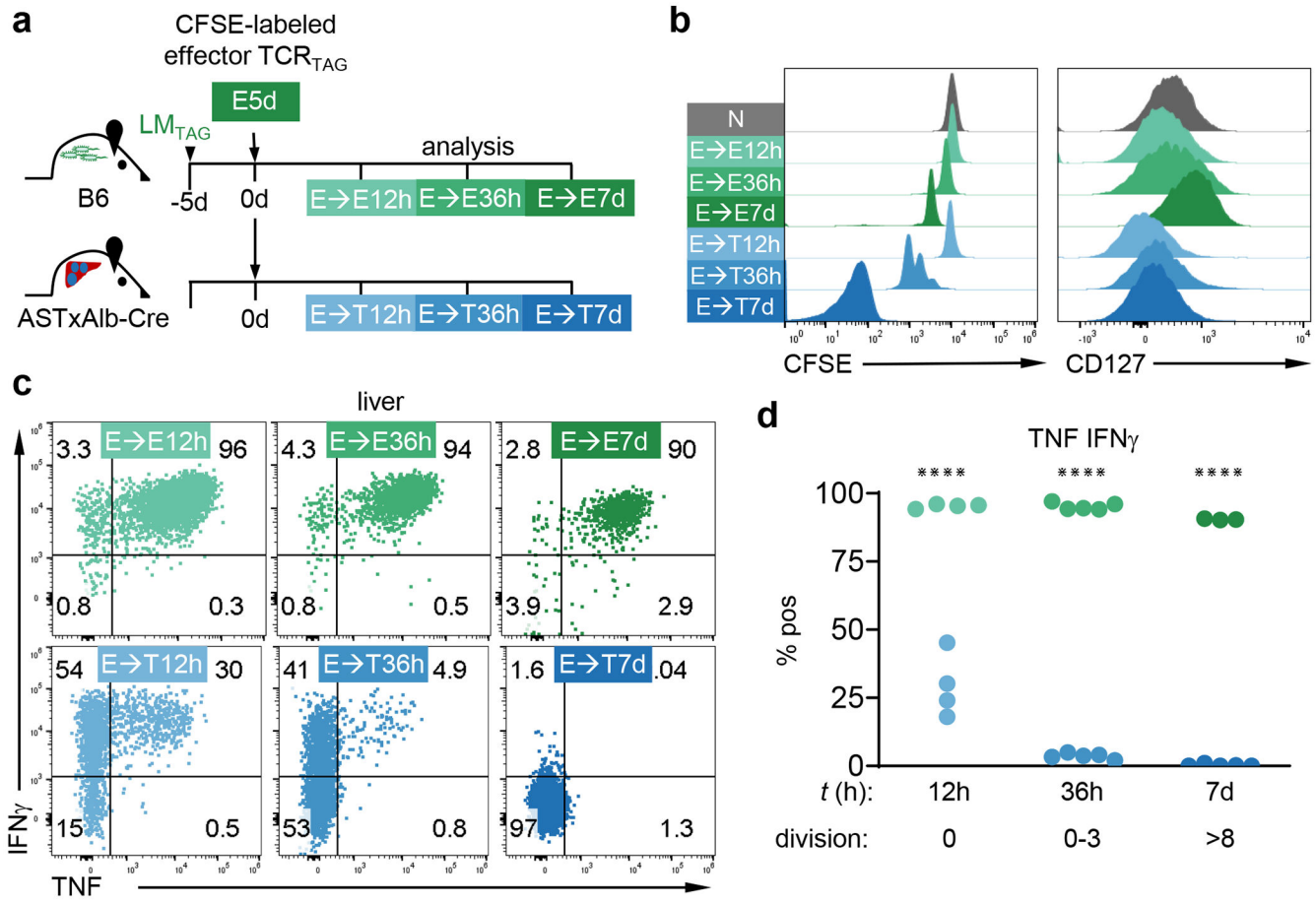

Figure 3|. Committed effector CD8 T cells rapidly lose function in tumor-bearing hosts.

a, Experimental scheme: committed effectors were generated by transferring naive TCR_{TAG} into LM_{TAG}-infected B6 mice and harvesting splenocytes 5 days (d) post transfer (E5d). E5d were CFSE-labeled and transferred into time-matched infected mice or tumor-bearing mice. TCR_{TAG} were re-isolated from infected (green) or tumor-bearing (blue) secondary recipients 12h, 36h, and 7d post-transfer. All flow plots are gated on live $CD8^+$ $Thy1.1^+$ cells. **b**, Representative histograms of CFSE dilution and CD127 expression from spleens of infected animals and livers of tumor-bearing mice with naive TCR_{TAG} (N; grey) shown for comparison. **c**, Representative dot plots of TCR_{TAG} IFNγ and TNF production after 4h *ex vivo* TAG peptide stimulation from livers of infected mice or liver-tumor bearing mice, with inset numbers indicating percentage of cells in each gate. Gates set based on no peptide stimulation controls. **d**, Summary plots of percentage $TNF^+IFN\gamma^+$ TCR_{TAG}. Each symbol represents an individual mouse with n=3-5 per group pooled from two experiments. ****P <0.0001 determined by two-way ANOVA with post hoc Tukey test.

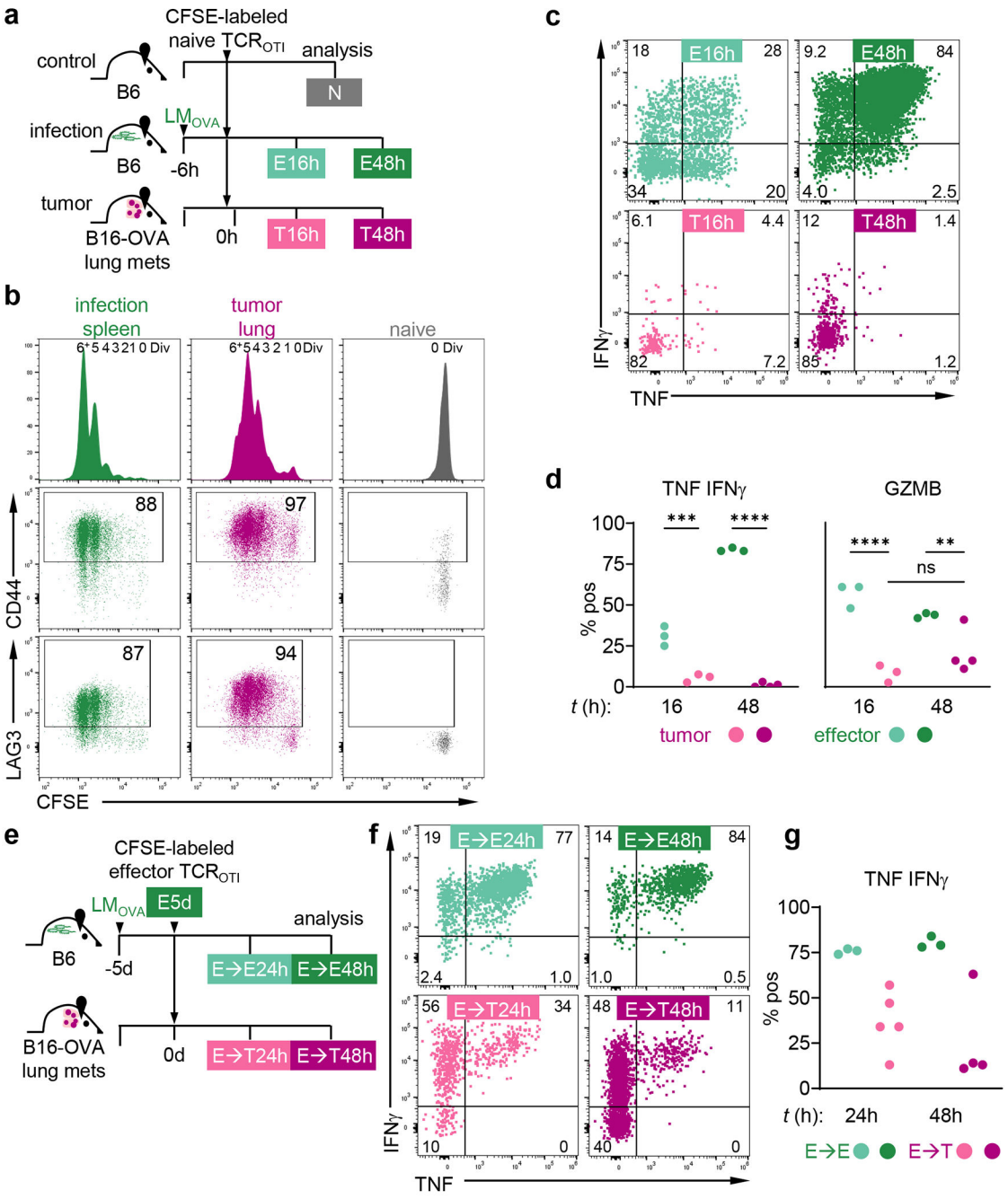

Figure 4|. Naive and effector TST robustly proliferate in mice with metastatic melanoma but lack effector function.

a, Experimental scheme: CFSE-labeled naive TCR_{OTI} (Ly5.1) were adoptively transferred into B6 (Ly5.2), LM_{OVA}-infected B6 (Ly5.2), or B6 (Ly5.2) with pulmonary B16-OVA metastases, and lymphocytes were re-isolated from infected spleens (green) or tumor lungs (pink) at 16h and 48h post-transfer for analysis by flow cytometry. **b,** TCR_{OTI} CFSE dilution (upper) with CD44 and LAG3 versus CFSE dilution (lower) at 48h shown in comparison to N, with inset numbers indicating percentage of cells in each gate. Gates

set based on N. Each plot shows data concatenated from 3-4 mice/group. **c**, TCR_{OTI} IFNγ and TNF production after 4h *ex vivo* OVA peptide stimulation, with inset numbers indicating percentage of cells in each gate. Gates set based on no peptide stimulation controls. **d**, Summary plots of percentage $TNF^+IFN\gamma^+$ TCR_{OTI} after 4h *ex vivo* OVA peptide stimulation and *ex* vivo GZMB expression. Each symbol represents an individual mouse. Two independent experiments were carried out with 3-4 mice/group. $^{**}P$=0.0012, $^{***}P$ =0.0005, and $^{****}P$ <0.0001 determined by two-way ANOVA with post hoc Tukey test. **e**, Experimental scheme: committed effectors were generated by transferring naive TCR_{OTI} into LM_{OVA}-infected B6 mice and harvesting splenocytes 5 days post transfer (E5d). E5d were CFSE-labeled and transferred into time-matched LM_{OVA}-infected B6 or B6 with pulmonary B16-OVA metastases. TCR_{OTI} were re-isolated from infected spleens (green) or lung tumors (pink) of secondary recipients 24h and 48h post-transfer. All flow plots are gated on live $CD8^+$ $Ly5.1^+$ cells. **f,** TCR_{OTI} IFNγ and TNF production after 4h *ex vivo* OVA peptide stimulation, with inset numbers indicating percentage of cells in each gate. Gates set based on no peptide stimulation controls. **g,** Summary plots of percentage $TNF^+IFN\gamma^+$ TCR_{OTI} where each symbol represents an individual mouse. $^{*}P$=0.017 and $^{**}P$=0.0023 determined by two-way ANOVA with post hoc Tukey test.

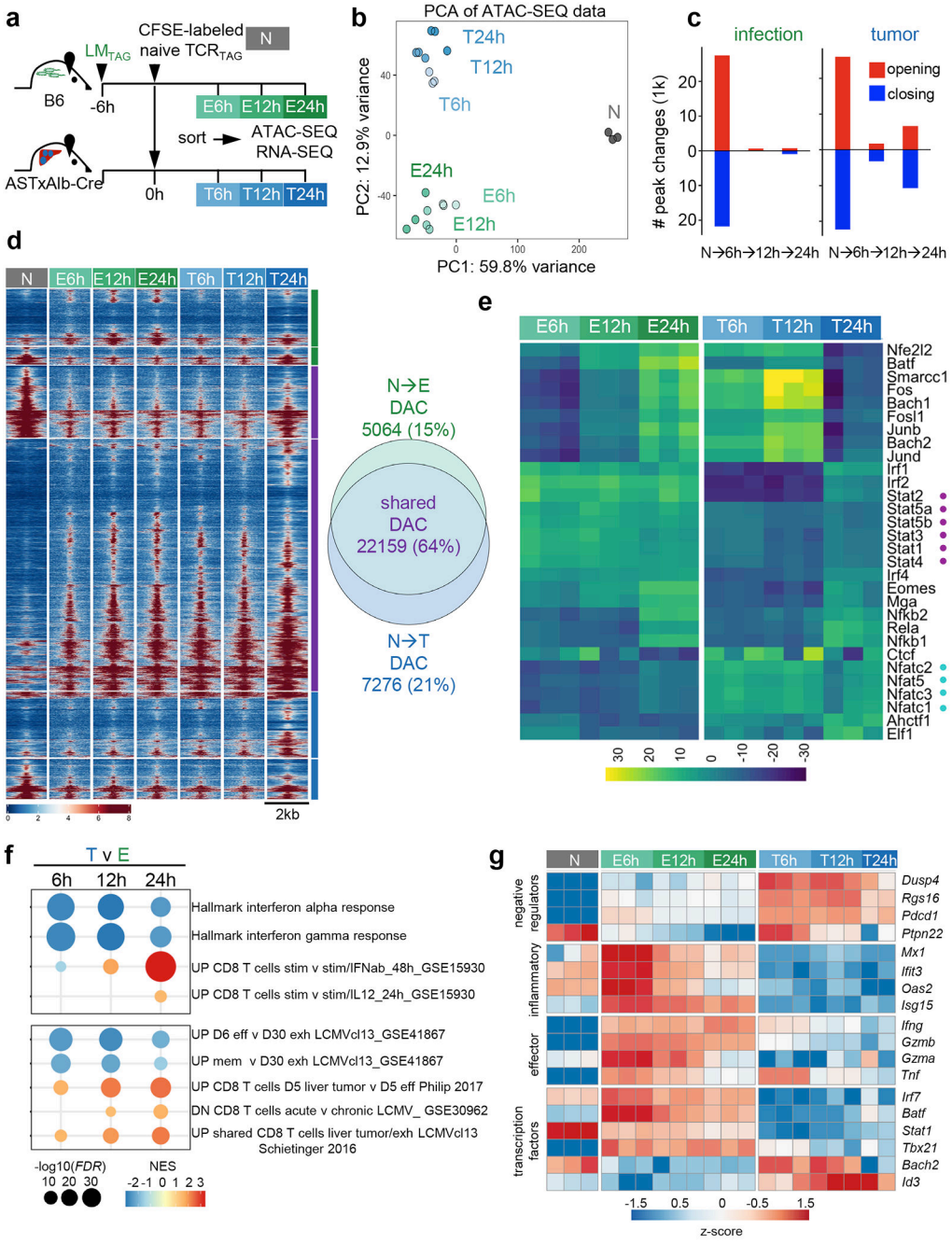

Figure 5|. Dysfunction-associated epigenetic programming begins prior to cell division.

a, Experimental scheme: CFSE-labeled naive TCR_{TAG} (Thy1.1) were adoptively transferred into LM_{TAG}-infected B6 (Thy1.2), or ASTxAlb-Cre (Thy1.2), and TCR_{TAG} were flow-sorted from spleens and livers at 6h, 12h, and 24h post-transfer (see Extended Data Fig. 5a). **b**, Principal component analysis (PCA) comparing chromatin accessibility in naive (N; grey) and TCR_{TAG} differentiating during acute infection (green) and in tumors (blue) at 6, 12, and 24h post-transfer by the top $25x10^3$ variable peaks. Each symbol represents a single biological replicate. **c**, Number differentially accessible chromatin peaks (DAC)

during each transition (opening peaks, red; closing peaks, blue; *FDR*<0.05). **d**, Chromatin accessibility heatmap. Each row represents one of 34,449 peaks (*FDR*<0.05, $|\log_2 FC| > 1.5$) displayed over 2kb window centered on the peak summit. Scale units are reads per genomic content (RPGC) normalized to 1x sequencing depth for 20 bp bins with blue indicating closed chromatin and red open chromatin. Peaks are ordered by membership within each subset shown in the Venn diagram (right) and hierarchical-clustering within the subset. Venn diagram showing DAC in TCR_{TAG} at early time points in infection, tumors, or shared in infection and tumors. **e,** Heatmap of chromVAR computed deviations z-score for the top 30 most variable transcription factor (TF) motifs enriched in DAC from TCR_{TAG} from tumors and infected mice at 6, 12, and 24h. Purple dots denote STAT TF family motifs enriched in effectors and blue dots denote NFAT TF family motifs enriched in TST. **f,** Gene set enrichment analysis (GSEA) on differentially-expressed genes in TCR_{TAG} from tumors (T) relative to infection (E) at 6, 12, and 24h. Color represents normalized enrichment score (NES) and circle size represents the negative $\log_{10}(FDR)$. **g,** Heatmap showing selected differential gene expression between naive TCR_{TAG} and TCR_{TAG} in tumors or infection at 6,12, and 24h (*FDR* <0.05, $|\log_2 FC| > 1$), z-score normalization across rows.

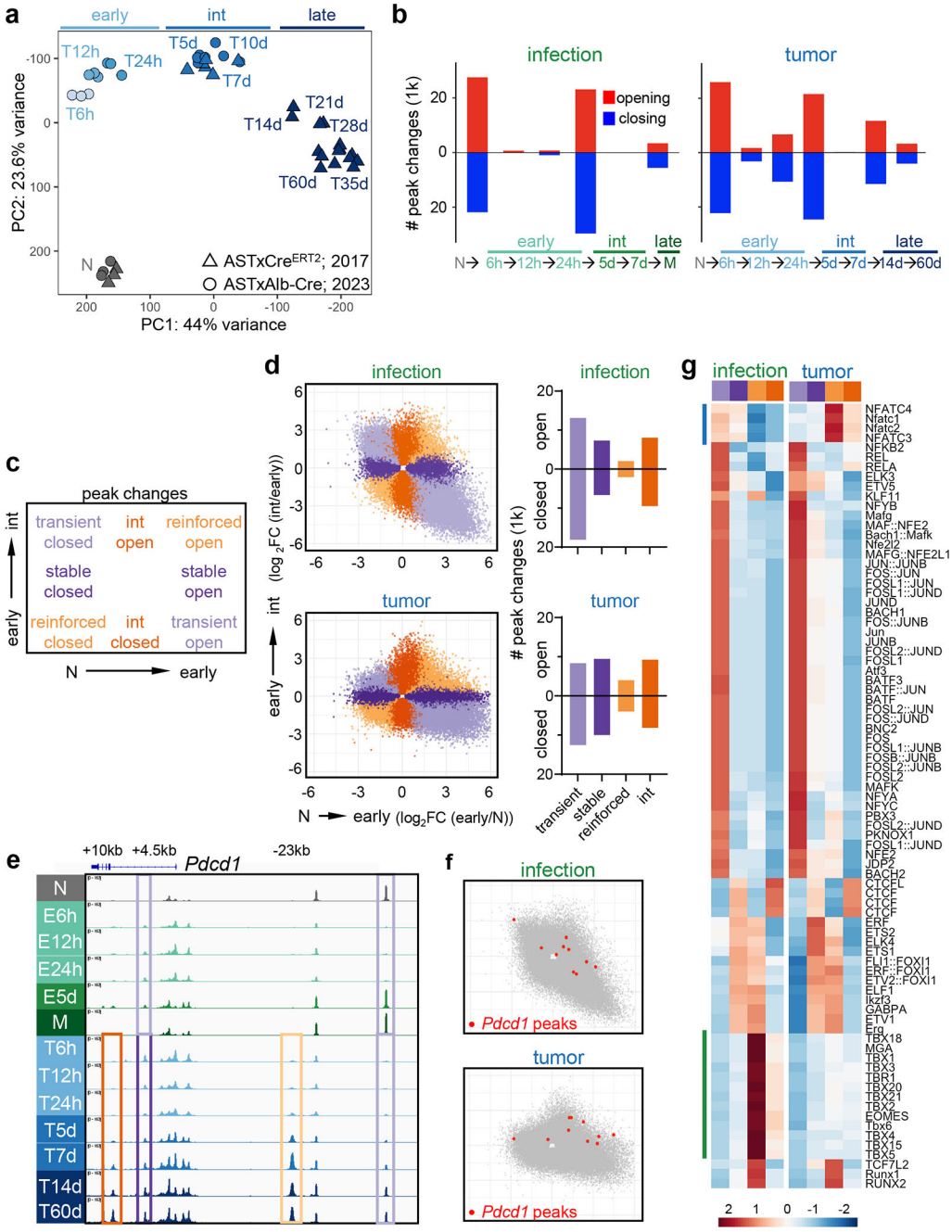

Figure 6|. Pre-division tumor-induced TST chromatin remodeling is reinforced with time and tumor antigen exposure.

a, PCA comparing chromatin accessibility in naive TCR_{TAG} (N) and TST after 6h, 12h and 24h (early), 5d, 7d, 10d (intermediate; int), 14d, 21d, 28d, 35d, and 60d+ (late). Circles: TCR_{TAG} in liver-tumor bearing ASTxAlb-Cre from the current study (2023) and triangles: TCR_{TAG} in pre- and malignant liver tumor-bearing ASTxAST-Cre^{ERT2}, previously published (2017)[5]. **b**, Number peak changes during CD8 T cell differentiation in infection (left) and tumors (right) across (opening peaks, red; closing peaks, blue) *FDR*<0.05). **c**,

Legend for parts d-g identifying scatterplot quadrants of peak changes during early (x-axis) versus later (y-axis) transitions**. d,** Upper panel: peak changes during naive (N) → early (E6h) transition (log_2FC E6h/N) versus early → int (E5d) transition (log_2FC E5d/E24h). Lower panel: peak changes during N→ early (T6h) transition (log_2FC T6h/N) versus early → int (T5d) transition (log_2FC T5d/T24h). Each point represents an individual peak colored as in c. To the right bar plots show number peaks in each quadrant (opening peaks above axis and closing peaks below axis; *FDR*<0.05 for either comparison). **e**, TCR_{TAG} *Pdcd1* locus accessibility profile across time points during infection and in liver tumors. Boxes highlighting peaks are colored as in c. The exhaustion-associated −23kb peak in *Pdcd1* is highlighted in light orange denoting an opening peak reinforced during tumor progression. Light purple boxes highlight transiently closed and open peaks. For T-TCR_{TAG}, the dark purple box highlights an opened peak maintained at later time points, and the dark orange box highlights a peak that opened at the later time points. **f**, Scatterplot highlighting individual *Pdcd1* peaks (red) relative to overall peaks (grey). **g,** Motif aNAlysis with Lisa (monaLisa) showing enriched transcription factor (TF) motifs for each set of peaks classified as in c, d during the early (N→6h) and intermediate (24h→5d) transitions in infection and tumor. Highlighted are NFAT TF family members, enriched in tumor reinforced and intermediate opening peaks, and T-box TF family members, enriched in infection reinforced and intermediate opening peaks.

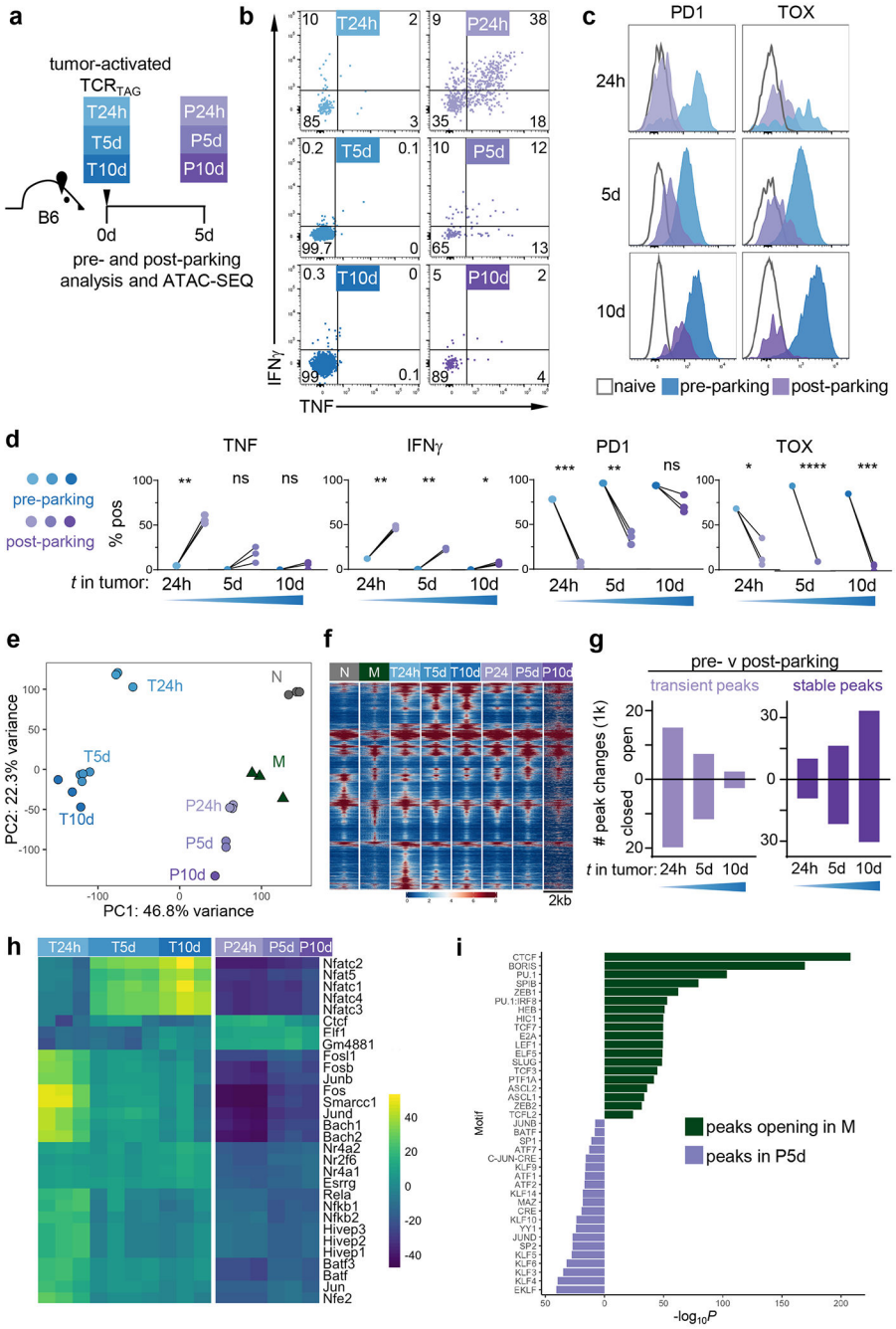

Figure 7|. Duration of tumor antigen exposure determines dysfunction stability and imprinting.

a, Experimental scheme: TCR_{TAG} adoptively transferred into ASTxAlb-Cre for 24h, 5d, or 10d (pre-parking) were isolated from tumors, transferred into tumor-free B6 mice, parked for 5d (post-parking), and then isolated from secondary hosts (P24h, P5d, P10d) and analyzed. **b,** Live $CD8^+$ $Thy1.1^+$ TCR_{TAG} analyzed pre- (left) and post-parking (right). IFN**γ** and TNF production after 4h *ex vivo* TAG peptide stimulation, with inset numbers indicating percentage of cells in each gate. Gates set based on no peptide stimulation controls. **c,** Histogram plots of pre-parking TCR_{TAG} (blue) and concatenated post-parking

samples (purple), with naive (N; open grey) for comparison. TCR_{TAG} were exposed to tumors for 24h (upper), 5d (middle), and 10d (lower) prior to transfer to tumor-free hosts. **d,** Summary plots show the percentage TNF^+, $IFN\gamma^+$, $PD1^+$, and TOX^+ pre-parking (for pooled donor TCR_{TAG} from 3-4 mice) and post-parking (each symbol represents an individual mouse). TNF: $^{**}P$=0.003. IFNγ: $^{**}P$=0.0013, 0.0011, and $^{*}P$=0.0191. PD1: $^{***}P$=0.0005, $^{**}P$=0.0049. TOX: $^{*}P$=0.037, $^{****}P$<0.0001, and $^{***}P$=0.0007. ns=not significant. Statistical significance determined for change from baseline by one sample Student's t-test. Two independent experiments were carried out with n=2-4 mice per group. **e,** Principal component analysis (PCA) comparing chromatin accessibility in naive (N; grey), memory, (M; green), TCR_{TAG} pre-parking (T24h, T5d, T10d; blue) and post-parking (P24h, P5d, P10d; purple) by the top $25x10^3$ variable peaks. Each symbol represents an individual biological replicate. **f**, Chromatin accessibility heatmap in naive (N), memory (M) and pre- and post-parking TCR_{TAG}. Each row represents one of 58,834 peaks (differentially accessible between at least one comparison; *FDR* <0.05, $|\log_2 FC| > 1.5$) displayed over 2kb window centered on the peak summit. **g,** Number of chromatin peaks that are transient or stable post-parking (determined as in Fig. 5c) relative to pre-parking. **h,** Heatmap of chromVAR computed deviations z-score for the top 30 most variable transcription factor (TF) motifs across TCR_{TAG} pre- and post-parking. **i,** Paired comparison of enriched TF motifs by HOMER between M and post-parking P5d TCR_{TAG}.